Journal of Fluids and Structures 100 (2021) 103173

Contents lists available at ScienceDirect

Journal of Fluids and Structures

journal homepage: www.elsevier.com/locate/jfs

Response of a plate in turbulent channel flow: Analysis of fluid–solid coupling

Sreevatsa Anantharamu, Krishnan Mahesh *

Aerospace Engineering and Mechanics, University of Minnesota - Twin Cities, Minneapolis, MN 55455, USA

ARTICLE INFO

Article history:
Received 8 April 2020
Received in revised form 28 August 2020
Accepted 21 October 2020
Available online xxxx

Keywords:
Direct numerical simulation
Fluid–structure interaction
fluid–solid coupling
Plate vibration
Turbulent channel flow
Spectral POD
One-way coupling

ABSTRACT

The paper performs simulation of a rectangular plate excited by turbulent channel flow at friction Reynolds numbers of 180 and 400. The fluid–structure interaction is assumed to be one-way coupled, i.e, the fluid affects the solid and not vice versa. We solve the incompressible Navier–Stokes equations using finite volume direct numerical simulation in the fluid domain. In the solid domain, we solve the dynamic linear elasticity equations using a time-domain finite element method. The obtained plate averaged displacement spectra collapse in the low frequency region in outer scaling. However, the high frequency spectral levels do not collapse in inner units. This spectral behavior is reasoned using theoretical arguments. The resonant vibration is stronger at the third natural frequency than at the first natural frequency. We explain this behavior by comparing the fluid and solid length scales. We further study the sources of plate excitation using a novel formulation. This formulation expresses the average displacement spectrum of the plate as an integrated contribution from the fluid sources within the channel. Analysis of the sources reveals that at the plate natural frequencies, the contribution of the fluid sources to the plate excitation peaks in the buffer layer. The corresponding wall-normal width is found to be $\approx 0.75\delta$. The integrated contribution of the overlap and outer regions together to the plate response is comparable to that from the buffer region for $Re_\tau = 180$ and exceeds the buffer region contribution for $Re_\tau = 400$. We analyze the decorrelated features of the sources using spectral Proper Orthogonal Decomposition (POD) of the net displacement source. We enforce the orthogonality of the modes in an inner product with a symmetric positive definite kernel. The dominant spectral POD mode contributes to the entire plate excitation. The contribution of the remaining modes from the different wall-normal regions undergo destructive interference resulting in zero net contribution. The envelope of the dominant mode further shows that the intensity of the sources peaks in the buffer region and the wall-normal width of the sources extend well into the outer region of the channel.

1. Introduction

The coupling between a turbulent flow and the resulting structural excitation is a problem of interest in marine, civil and aerospace engineering. In this paper, we investigate this coupling in a canonical setting — linear one-way coupled (fluid affects solid, but not vice versa) response of an elastic plate in turbulent channel flow (Pope, 2001) due to wall-pressure fluctuations alone. Specifically, we address the question — how much do the fluid sources at different

* Corresponding author.
E-mail addresses: anant035@umn.edu (S. Anantharamu), kmahesh@umn.edu (K. Mahesh).

https://doi.org/10.1016/j.jfluidstructs.2020.103173
0889-9746/

wall-normal locations contribute to the plate excitation for different frequencies, and what are the salient features of these fluid sources? We answer this question with a novel formulation that combines Direct Numerical Simulation (DNS) data, Green's function formulation and spectral Proper Orthogonal Decomposition (POD). For brevity, we will sometimes refer to wall-pressure fluctuations as just wall-pressure.

The one-way coupling between the fluid sources and plate excitation can be broken into two parts: (i) fluid source–wall-pressure fluctuation coupling, and (ii) wall-pressure fluctuation–plate excitation coupling. Note that we neglect the wall-shear stress contribution to the plate forcing. We further classify the techniques to investigate the fluid source–wall-pressure fluctuation coupling into — scaling variables-based, Green's function-based and conditional averaging-based techniques. We discuss some features of the wall-pressure fluctuation sources identified by each of these techniques.

Identification of the scaling variables for the power-spectral density (PSD)/wavenumber spectrum of wall-pressure fluctuation yields qualitative information of the wall-normal region of the fluid sources. The wall-pressure PSD in the low ($\omega\delta/u_\tau < 5$), mid ($5 < \omega\delta/u_\tau < 100$) and high frequency ranges ($\omega\delta/u_\tau > 0.3Re_\tau$) scale with the potential flow variables (ρ_f, δ^*, U_o), outer flow variables (ρ_f, δ, τ_w), and inner flow variables (ρ_f, ν_f, τ_w), respectively (Farabee and Casarella, 1991), where ω is the angular frequency, ρ_f is the fluid density, δ is the boundary layer thickness, δ^* is the displacement thickness of the boundary layer, U_o is the centerline velocity, τ_w is the wall-shear stress, $u_\tau = \sqrt{\tau_w/\rho_f}$ is the friction velocity, ν_f is the kinematic viscosity of the fluid, and the friction Reynolds number Re_τ is defined as $u_\tau\delta/\nu_f$. Thus, the sources responsible for the low, mid and high frequency wall-pressure fluctuations are predominantly in the potential, outer and inner region of the turbulent boundary layer, respectively.

The Green's function-based techniques (Chang III et al., 1999; Anantharamu and Mahesh, 2020) yield quantitative information of the sources of wall-pressure fluctuation. The premultiplied streamwise wavenumber spectrum and the PSD of the wall-pressure fluctuations in a turbulent channel show peaks at $\lambda_x^+ = 300$ (Panton et al., 2017) and $\omega^+ \approx 0.35$ (Hu et al., 2006) for $Re_\tau = 180 - 5000$, respectively, where λ_x is the streamwise wavelength, and $+$ indicates normalization with viscous units (ν_f and u_τ). The dominant contributors to this inner peak are in the buffer region of the channel (Anantharamu and Mahesh, 2020). The approach of Anantharamu and Mahesh (2020) that identified this dominant contribution (i) combines DNS data with the Green's function formulation to express the wall-pressure PSD ($\phi_{pp}(\omega)$) as integrated contribution ($\Gamma(r, s, \omega)$) from all wall-parallel plane pairs, $\phi_{pp}(\omega) = \iint_{-\delta}^{+\delta} \Gamma(r, s, \omega)\,\mathrm{d}r\,\mathrm{d}s$, (ii) accounts for the relative phase difference between the contributions from different wall-parallel planes neglected in the previous Green's function approach of Chang III et al. (1999), and (iii) yields a distribution of sources in the wall-normal direction instead of a wall-normal region as indicated by the scaling variables. Further, the methodology identified decorrelated features of wall-pressure fluctuation sources using spectral Proper Orthogonal Decomposition (POD). The identified dominant wall-pressure source at the linear and premultiplied wall-pressure PSD peak frequency resembled tall and inclined patterns, respectively.

The conditional averaging-based technique (Ghaemi and Scarano, 2013) yields patterns of the flow structure that are correlated to a particular wall-pressure fluctuation event. The time history of the wall-pressure fluctuation signal at a point on the wall shows occasional positive and negative high amplitude wall-pressure peaks. The conditionally averaged flow fields show coupling between a hairpin vortex and the high amplitude peaks (Ghaemi and Scarano, 2013). The flow structure responsible for the positive and negative high amplitude wall-pressure peak at a point are the sweep and ejection event occurring above it, respectively. The ejection event responsible for the negative peak occurs upstream of the hairpin head in between the quasi-streamwise vortices. The sweep event that leads to the positive peak occurs downstream of the hairpin head.

The dynamic linear elasticity equations describe the wall-pressure fluctuation–plate excitation coupling. This one-way coupled FSI approach is valid for small linear deformation ($du_\tau/\nu_f < 1$) of the plate, where d is the wall-normal displacement. The approach generally uses (i) plate theories (e.g. Poisson–Kirchhoff) to describe the deformation, and modal superposition to obtain the response, (ii) frequency domain since steady state response is usually the quantity of interest, and (iii) a model wavenumber-frequency spectrum (Corcos, 1964; Chase, 1980; Hwang, 1998) for the spatially homogeneous wall-pressure fluctuations as input. Note that the model wavenumber-frequency spectrum usually requires a model PSD (Bull, 1967; Smol'Iakov and Tkachenko, 1991; Goody, 2004). The mode shapes and natural frequencies of the plate required to perform modal superposition can be obtained analytically for simple boundary conditions and geometry. For complicated boundary conditions and geometry, Finite Element Method (FEM) is used to compute the modal decomposition.

The wall-pressure fluctuation–plate excitation coupling has been previously investigated in wavenumber space (Hwang and Maidanik, 1990; Blake, 2017). The modal force PSD of the plate can be expressed as the wavenumber integral (Blake, 2017)

$$\begin{aligned} \phi_{f_j f_j}(\omega) &= \int\!\!\int_{-\infty}^{+\infty} \varphi_{pp}(k_1, k_3, \omega)|S_j(k_1, k_3)|^2 \mathrm{d}k_1\,\mathrm{d}k_3, \\ S_j(k_1, k_3) &= \int_a^{a+L_x}\int_b^{b+L_z} S_j(x, z) e^{i(k_1 x + k_3 z)}\,\mathrm{d}x\,\mathrm{d}z, \end{aligned} \tag{1}$$

where a and b are the origins of the plate in the streamwise and spanwise directions, L_x and L_z are the lengths of the plate in the streamwise and spanwise directions, $\phi_{f_j f_j}(\omega)$ is the modal force PSD of the jth mode shape, $\varphi_{pp}(k_1, k_3, \omega)$ is the

Table 1
Fluid and solid domain extents.

$L_x^f \times L_y^f \times L_z^f$	$L_x^s \times L_y^s \times L_z^s$
$6\pi\delta \times 2\delta \times 2\pi\delta$	$(6\pi/5)\,\delta \times 0.004\delta \times (2\pi/5)\,\delta$

wall-pressure wavenumber-frequency spectrum and $|S_j(k_1, k_3)|^2$ is the modal shape function. From the above equation, we observe that the modal shape function couples the wall-pressure wavenumber-frequency spectrum to the modal force. The relative contribution of different wavenumber regions to the modal force spectra depends on the mode order (j), boundary conditions, and the ratio of the streamwise modal wavenumber ($k_{m,j}$) to the convective wavenumber at the natural frequency of the mode (Hwang and Maidanik, 1990). The high streamwise wavenumber ($k_1/k_{m,j} \gg 1$) portion of $|S_j(k_1, k_3)|^2$ decays as k_1^{-6}, k_1^{-4} and k_1^{-2} for clamped, simply supported and free boundary conditions on all edges (Blake, 2017). Thus, plates with free boundary conditions accept more of the high streamwise wavenumber component of the wall-pressure fluctuations. Further, special wall-pressure fluctuation models that separately approximate the high and low wavenumber portion of the wall-pressure fluctuation wavenumber-frequency spectrum can be derived and used to obtain the response of plates (Hambric et al., 2004). Hambric et al. (2004) showed good agreement between FEM response of a plate excited by the modified Corcos model of Hwang (1998) and an equivalent edge forcing model which only models the convective component in the modified Corcos model for a plate with three edges clamped and one edge free. This shows the importance of the convective region of wall-pressure fluctuation spectrum for plates with free boundary conditions. For a plate with all four edges clamped, FEM response from a low wavenumber excitation model showed good agreement with the modified Corcos model, thus highlighting the dominance of low wavenumber contribution for clamped boundary condition.

Experiments by Zhang et al. (2017) have shown coupling between flow structures and the response of a compliant wall in a turbulent channel flow. The large positive and negative deformation of the compliant wall is coupled to the ejection and sweep events, respectively, occurring above it (Zhang et al., 2017). Conditionally averaged flow fields show that these events are related to the high amplitude pressure peaks and hairpin vortices that surround the local deformation of the compliant wall. For large deformation of the compliant wall, the plate deflection affects the near-wall turbulence. The compliant wall deflection into the buffer layer breaks the near-wall streaks and the associated quasi-streamwise vortices, and induces more spanwise coherence (Rosti and Brandt, 2017).

In this paper, we develop a formulation to obtain the wall-normal distribution of intensity and relative phase of the fluid sources responsible for the plate excitation. Previous research works do not yield such quantitative information of the fluid sources. The main idea is to express the plate averaged displacement PSD as a double wall-normal integral of the 'net displacement source' cross-spectral density (CSD) $\Gamma^a(r, s, \omega)$ across the height of the channel. The analysis framework combines the volumetric DNS data, Green's function solution of the pressure fluctuation and modal superposition, and builds on the previous work of Anantharamu and Mahesh (2020). We then apply the framework to explain the one-way coupled FSI simulation results of an elastic plate in turbulent channel flow at $Re_\tau = 180$ and 400. The fluid and solid simulations make use of finite volume DNS and time-domain FEM, respectively. Further, the decorrelated fluid sources that contribute the most to plate response are obtained using spectral POD of the net displacement source CSD.

The organization of the paper is as follows: In Section 2, we describe the computational domain, mesh resolution, and the FSI simulation details. Section 3 discusses the novel one-way coupling analysis framework. In Section 4.1, we discuss the obtained one-way coupled FSI results. We compare the fluid and solid length scales for the first three modes in Section 4.2. Section 4.3 discusses the spectral features of the net displacement source CSD and in Section 4.4, we identify the decorrelated features of the fluid source using spectral POD. Finally, we summarize the results in Section 5.

Note that x, y and z denote the streamwise, wall-normal and spanwise coordinates, respectively. Superscripts/subscripts f and s denote fluid and solid quantities, respectively.

2. FSI simulation details

2.1. Computational domain

Fig. 1 shows a schematic of the fluid and solid computational domain and Table 1 shows the domain extents. The fluid computational domain is a Cartesian box of size $L_x^f \times L_y^f \times L_z^f$. We choose $L_x^f = 6\pi\delta$, $L_y^f = 2\delta$ and $L_z^f = 2\pi\delta$, where δ is the half channel height. Long streamwise and spanwise domains include the contribution of large scale structures to pressure fluctuations. The solid computational domain is a rectangular plate clamped on all sides placed at the bottom wall of the channel. The plate is flush with the bottom wall and centered. The length (L_x^s), width (L_z^s), and thickness (L_y^s) of the plate is $6\pi\delta/5$, $2\pi\delta/5$ and 0.004δ, respectively. The smaller dimension of the plate ensures that the pressure fluctuations with wavelengths larger than the plate dimensions are present in the computational box. Thus, we include the low wavenumber ($k_1 \ll k_{m,j}$) wall-pressure fluctuation contribution to plate excitation.

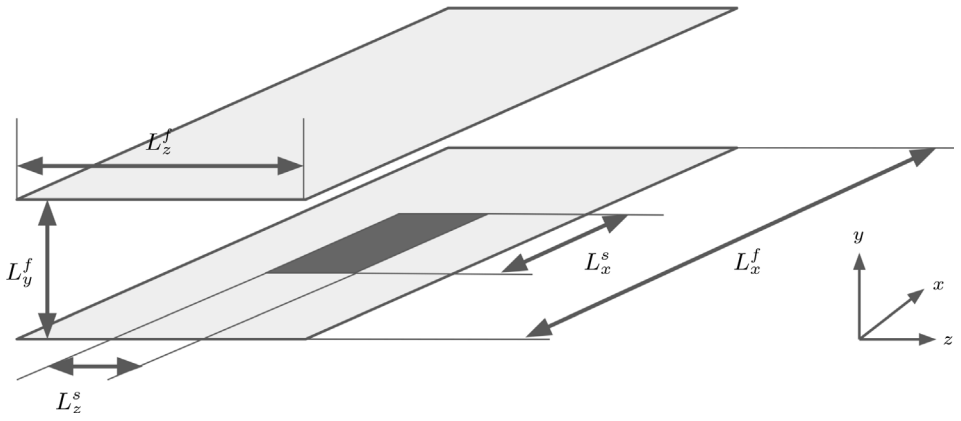

Fig. 1. Computational domain of the FSI simulation.

Table 2
Fluid and solid mesh sizes and resolution of the FSI simulation. Note that the fluid and solid meshes match at the interface.

Re_τ	$N_x^f \times N_y^f \times N_z^f$	$N_x^s \times N_y^s \times N_z^s$	Δx^+	Δz^+	Δy_w^{f+}	Δy_c^{f+}
180	720 × 176 × 330	144 × 1 × 66	4.7	3.4	0.27	4.4
400	1388 × 288 × 660	288 × 1 × 132	5.4	3.8	0.37	5.9

2.2. Fluid DNS

We solve the incompressible Navier–Stokes equations in the fluid domain using the collocated finite volume method of Mahesh et al. (2004) in a frame of reference moving with the bulk velocity of the fluid as done by Bernardini et al. (2013). This lead to better prediction of the high frequency component of the pressure spectra. The walls in the channel are assumed to be rigid in the fluid calculation. For time integration, we use the Crank–Nicholson scheme. Overall, the method is second order accurate in space and time, and non-dissipative. The algorithm conserves kinetic energy discretely. This ensures stability of the algorithm at high Reynolds numbers without adding numerical dissipation. We perform the DNS using the in-house flow solver — MPCUGLES.

The fluid mesh is Cartesian. The mesh is uniform in the streamwise and spanwise directions. In the wall-normal direction, we use a non-uniform hyperbolic tangent spacing to cluster control volumes near the wall. Table 2 shows the fluid mesh sizes and resolutions for both Re_τ. The streamwise spacing (Δx^+), spanwise spacing (Δz^+), the wall-normal spacing near the wall (Δy_w^{f+}) and channel centerline (Δy_c^{f+}) is fine enough to resolve the fine-scale features of wall turbulence. The timestep of the fluid simulation is $5 \times 10^{-4}\delta/u_\tau$ for both Re_τ. The velocity (U_b/u_τ) of the moving reference frame is 15.8 and 17.8 in the streamwise direction for $Re_\tau = 180$ and 400, respectively. We employ a slip velocity boundary condition (equal to $-U_b/u_\tau$) at the top and bottom wall. For pressure, we use a zero Neumann boundary condition at the top and bottom wall. In the streamwise and spanwise directions, we use periodic boundary conditions for both velocity and pressure. For validation of the fluid DNS, we refer the reader to Anantharamu and Mahesh (2020).

2.3. Solid simulation

We solve the three-dimensional dynamic linear elasticity equations in the solid domain with the continuous Galerkin Finite Element Method (abbreviated as just FEM). We perform the solid simulation using the validated in-house solid solver — MPCUGLES-SOLID. We use second-order polynomials in each element to represent the solution and trapezoidal rule for the time integration of the equations. We solve the resulting matrix problem using the parallel sparse direct solver package SuperLU_DIST (Li and Demmel, 2003). We compute the sparse factors once at the beginning of the simulation and use it to obtain the solution at each timestep. For thin plate problems, we found the sparse direct solvers to be at least 20 times faster than the state of the art iterative solvers (multigrid preconditioned conjugate gradient on the scaled thickness preconditioned system (Klöppel et al., 2011)). This is because the matrix problem arising from the discretization of thin plate using solid elements is extremely ill-conditioned. Therefore, even the state of the art iterative solvers require a large number of iterations to converge to a specified tolerance. For validation of the structural solver, we refer the reader to Appendix B.

We non-dimensionalize the structural equations with the half-channel height (δ), fluid density (ρ_f), and friction velocity (u_τ). The non-dimensional properties of the plate are shown in Table 3. We describe the procedure used to arrive at the values in Table 3 and the physical significance behind the choice in Appendix A.

Table 3
Non-dimensional properties of the plate.

Young's modulus $(E/(\rho_f u_\tau^2))$	6.88×10^9
Poisson ratio (ν_s)	0.4
Solid density (ρ_s/ρ_f)	1.17×10^3

We incorporate damping using Rayleigh damping with mass proportional damping coefficient of 2.25. The structural loss factor with the chosen mass proportional damping is around 0.05 at the first natural frequency. The solid simulation timestep is the same as the fluid DNS.

The solid mesh is Cartesian and composed of 27-node hexahedral elements. Table 2 gives the dimensions of the mesh. Since the plate is of high aspect ratio, we only use one element in the thickness direction. Further, the fluid and solid meshes match at the interface. Thus, no special load transfer strategy is required. We set the displacement of the nodes on all four sides of the plate to zero and apply the rigid wall DNS wall-pressure fluctuations onto the top surface of the plate.

The fluid DNS is first run until it reaches a statistically stationary state. Then, the one-way coupled FSI simulation is run for a total time of $30\delta/u_\tau$ units for $Re_\tau = 180$ and $23\delta/u_\tau$ units for $Re_\tau = 400$. For $Re_\tau = 180$ and 400, we discard the first $15\delta/u_\tau$ and $8\delta/u_\tau$ time units of the solid response, respectively, as it contains the initial transient response of the solid. We use the remaining $15\delta/u_\tau$ time units for $Re_\tau = 180$ and $15\delta/u_\tau$ for $Re_\tau = 400$ to compute the statistics of the plate response.

3. Analysis framework

3.1. Theory

The goal is to express the plate averaged displacement PSD as a double integral over all the wall-parallel plane pairs. To accomplish this, we first express the steady-state component of the bottom wall displacement $d(x, -\delta, z, t)$ as a wall-normal integral,

$$d(x, -\delta, z, t) = \int_{-\delta}^{+\delta} f_d(x, y, z, t)\mathrm{d}y. \tag{2}$$

Here, $f_d(x, y, z, t)$ is called the 'net displacement source' (exact form is derived later). It gives the contribution of each wall-parallel plane to the surface displacement of the plate. We define the plate averaged displacement PSD $\phi_{dd}^a(\omega)$ as

$$\begin{aligned} \phi_{dd}^a(\omega) &= \frac{1}{A_p}\iint_{\Gamma_{fs}} \phi_{dd}(x, -\delta, z, \omega)\,\mathrm{d}x\,\mathrm{d}z, \\ \phi_{dd}(x, -\delta, z, \omega) &= \frac{1}{2\pi}\int_{-\infty}^{+\infty} \langle d^*(x, -\delta, z, t) d(x, -\delta, z, t+\tau)\rangle e^{-i\omega\tau}\,\mathrm{d}\tau, \end{aligned} \tag{3}$$

where $\phi_{dd}(x, -\delta, z, \omega)$ is the displacement PSD at a point $(x, -\delta, z)$ on the surface of the plate, $\langle\cdot\rangle$ denotes ensemble average, A_p is the area of the plate, and Γ_{fs} is the plate surface. Note that the PSD ϕ_{dd} is independent of time t because we include only the steady-state component of the plate displacement $d(x, -\delta, z, t)$, which is stationary in time due to the stationary wall-pressure fluctuations.

We can then relate the plate averaged displacement PSD $\phi_{dd}^a(\omega)$ to the net displacement source $f_d(x, y, z, t)$ using Eqs. (2) and (3) as

$$\begin{aligned} \phi_{dd}^a(\omega) &= \iint_{-\delta}^{+\delta} \Gamma^a(r, s, \omega)\,\mathrm{d}r\,\mathrm{d}s, \\ \Gamma^a(r, s, \omega) &= \frac{1}{A_p}\int_{\Gamma_{fs}} \left(\frac{1}{2\pi}\int_{-\infty}^{+\infty} \langle f_d^*(x, r, z, t) f_d(x, s, z, t+\tau)\rangle e^{-i\omega\tau}\,\mathrm{d}\tau\right)\mathrm{d}x\,\mathrm{d}z, \end{aligned} \tag{4}$$

where $\Gamma^a(r, s, \omega)$ is the plate averaged CSD of $f_d(x, y, z, t)$. The function $\Gamma^a(r, s, \omega)$ yields the contribution of each wall-parallel plane pair to the PSD $\phi_{dd}^a(\omega)$ for different frequencies. Note that the CSD does not depend on time t because, like the steady-state component of the plate displacement, the net displacement source is also stationary in time.

We obtain $f_d(x, y, z, t)$ as follows. First, we express the total (steady-state and transient) displacement $\tilde{d}(x, -\delta, z, t)$ in the modal basis as

$$\tilde{d}(x, -\delta, z, t) = \sum_{j=1}^{\infty} \tilde{d}_j(t)\,\varphi_j(x, -\delta, z), \tag{5}$$

where, $\varphi_j(x, -\delta, z)$ is the wall-normal component of the jth mode shape on the top surface of the plate, and $\tilde{d}_j(t)$ is the component of the $\tilde{d}$ along the jth mode shape. Then, we separate $\tilde{d}_j(t)$ into steady-state ($d_j(t)$) and transient ($\hat{d}_j(t)$) component as $\tilde{d}_j(t) = d_j(t) + \hat{d}_j(t)$. The steady-state component of the displacement is then

$$d(x, -\delta, z, t) = \sum_{j=1}^{\infty} d_j(t)\, \varphi_j(x, -\delta, z). \tag{6}$$

To obtain the expression for $\tilde{d}_j(t)$, we assume zero initial displacement and velocity of the plate, Rayleigh damping model to account for the damping of the plate, and obtain the below solution using the Duhamel integral (Bathe, 2006),

$$\tilde{d}_j(t) = \frac{1}{\bar{\omega}_j} \int_0^t f_j(\tau) e^{-\xi_j \omega_j (t-\tau)} \sin\left(\bar{\omega}_j\,(t-\tau)\right)\, \mathrm{d}\tau, \tag{7}$$

where $\bar{\omega}_j = \omega_j \sqrt{1-\xi_j^2}$, and $f_j(t)$ is the modal force of the jth mode shape of the plate given by

$$f_j(t) = -\iint_{\Gamma_{fs}} p(x, -\delta, z, t) \varphi_j(x, -\delta, z)\, \mathrm{d}x\, \mathrm{d}z, \tag{8}$$

and $\xi_j = (\alpha/\omega_j + \beta\omega_j)/2$. Here, α and β are the Rayleigh damping coefficients. We separate $\tilde{d}_j(t)$ into steady-state and transient components by Fourier transforming $f_j(t)$ in Eq. (10) and carrying out some algebraic manipulations,

$$\begin{aligned} \tilde{d}_j(t) = & \underbrace{\int_{-\infty}^{+\infty} \frac{\hat{f}_j(\omega)}{\left(\omega_j^2 - \omega^2\right) + 2i\xi_j\omega_j\omega} e^{i\omega t}\, \mathrm{d}\omega}_{steady-state} + \\ & \underbrace{e^{-\xi_j\omega_j t} \int_{-\infty}^{+\infty} \frac{\hat{f}_j(\omega)}{\left(\omega_j^2 - \omega^2\right) + 2i\xi_j\omega_j\omega} \left(cos\left(\bar{\omega}_j t\right) + \left(\frac{\xi_j\omega_j + i\omega}{\bar{\omega}_j}\right) sin\left(\bar{\omega}_j t\right)\right) \mathrm{d}\omega}_{transient}, \end{aligned} \tag{9}$$

where $\hat{f}_j(\omega) = (1/(2\pi)) \int_{-\infty}^{+\infty} f_j(\tau) e^{i\omega\tau}\, \mathrm{d}\tau$. From the above equation, we observe that the steady-state component is persistent, whereas the transient component decays exponentially with time. The steady state component $d_j(t)$ is then

$$d_j(t) = \int_{-\infty}^{+\infty} \frac{\hat{f}_j(\omega)}{\left(\omega_j^2 - \omega^2\right) + 2i\xi_j\omega_j\omega} e^{i\omega t}\, \mathrm{d}\omega. \tag{10}$$

To express $p(x, -\delta, z, t)$ in Eq. (8) as a wall-normal integral, we use the pressure fluctuation Poisson equation,

$$-\nabla^2 p = f = \rho_f \left(2\frac{\partial U_i^f}{\partial x_j} \frac{\partial u_j^{f'}}{\partial x_i} + \frac{\partial^2}{\partial x_i \partial x_j} \left(u_i^{f'} u_j^{f'} - \overline{u_i^{f'} u_j^{f'}} \right) \right), \tag{11}$$

where U_i^f and $u_i^{f'}$ are the mean and fluctuating fluid velocities, respectively. Neglecting the Stokes contribution, we use a zero Neumann boundary condition at the top and bottom walls for the pressure fluctuations. This is reasonable as the Stokes component of wall-pressure fluctuations is small at high Reynolds number (Hoyas and Jiménez, 2006). To obtain a unique solution, we set the average of the pressure fluctuations at the top and bottom wall to zero at all times. The solution to the pressure fluctuations $p(x, -\delta, z, t)$ at the bottom wall is then,

$$\begin{aligned} p(x, -\delta, z, t) &= \int_{-\delta}^{+\delta} f_G(x, y, z, t)\, \mathrm{d}y, \\ f_G(x, y, z, t) &= \iint_{-\infty}^{+\infty} G(-\delta, y, k) \hat{f}(k_1, y, k_3, t) e^{i(k_1 x + k_3 z)} \mathrm{d}k_1\, \mathrm{d}k_3, \\ k &= \sqrt{k_1^2 + k_3^2}, \\ G(r, s, k) &= \begin{cases} \frac{\cosh(k(s-\delta))\cosh(k(r+\delta))}{2k\sinh(k\delta)\cosh(k\delta)}, & r \le s, \\ \frac{\cosh(k(s+\delta))\cosh(k(r-\delta))}{2k\sinh(k\delta)\cosh(k\delta)}, & r > s, \end{cases} \end{aligned} \tag{12}$$

where $f_G(x, y, z, t)$ is termed the 'net source' function (Anantharamu and Mahesh, 2020), $G(-\delta, y, k)$ is the Green's function, and $\hat{f}(k_1, y, k_3, t)$ is the multidimensional Fourier transform of the source terms $f(x, y, z, t)$ defined as

$$\hat{f}(k_1, y, k_3, t) = \frac{1}{(2\pi)^2} \iint_{-\infty}^{+\infty} f(x, y, z, t) e^{-i(k_1 x + k_3 z)} \mathrm{d}x\, \mathrm{d}z. \tag{13}$$

We call $f_G(x, y, z, t)$ the 'net source' function because it includes contributions from all wavenumbers and the Green's function. Combining Eqs. (6), (8), (10), and (12), we obtain the required expression for the net displacement source $f_d(x, y, z, t)$ as

$$f_d(x, y, z, t) = \sum_{j=1}^{\infty} \left(\int_{-\infty}^{+\infty} \frac{\hat{r}_j(y, \omega)}{\left(\omega_j^2 - \omega^2\right) + i2\xi_j\omega_j\omega} e^{i\omega t} \, \mathrm{d}\omega \right) \varphi_j(x, -\delta, z), \tag{14}$$

where $\hat{r}_j(y, \omega) = 1/(2\pi) \int_{-\infty}^{+\infty} r_j(y, t) e^{-i\omega t} \, \mathrm{dt}$, and $r_j(y, t)$ is given by

$$r_j(y, t) = \iint_{\Gamma_{fs}} f_G(x, y, z, t) \varphi_j(x, -\delta, z) \, \mathrm{dx} \, \mathrm{dz}. \tag{15}$$

To obtain the contribution from the cross-correlation of the fluid sources with a particular plane $y = r$ to the plate averaged response PSD, we integrate $\Gamma^a(r, s, \omega)$ along s to obtain $\Psi^a(r, \omega)$,

$$\Psi^a(r, \omega) = \int_{-\delta}^{+\delta} \Gamma^a(r, s, \omega) \, \mathrm{ds}. \tag{16}$$

It can be shown that $\Psi_a(r, \omega)$ is the plate averaged wall displacement–net displacement source CSD,

$$\Psi^a(r, \omega) = \frac{1}{A_p} \int_{\Gamma_{fs}} \left(\frac{1}{2\pi} \int_{-\infty}^{+\infty} \langle f_d^*(x, r, z, t) d(x, -\delta, z, t + \tau) \rangle e^{-i\omega\tau} \, \mathrm{d}\tau \right) \mathrm{dx} \, \mathrm{dz}. \tag{17}$$

Further, the plate averaged wall displacement–net displacement source CSD relates to the plate averaged displacement PSD $\phi_{dd}^a(\omega)$ as

$$\phi_{dd}^a(\omega) = \int_{-\delta}^{+\delta} \Psi^a(r, \omega) \, \mathrm{dr} = \int_{-\delta}^{+\delta} Re\left(\Psi^a(r, \omega)\right) \, \mathrm{dr}, \tag{18}$$

where $Re(\cdot)$ is the real part of $\cdot$.

We relate the plate averaged net displacement source CSD $\Gamma_a(r, s, \omega)$ to the four-dimensional CSD of the pressure fluctuation source terms $\varphi_{ff}(r, s, k_1, k_3, \omega)$ as follows. The four-dimensional CSD $\varphi_{ff}(r, s, k_1, k_3, \omega)$ is defined as

$$\varphi_{ff}(r, s, k_1, k_3, \omega) = \frac{1}{(2\pi)^3} \iiint_{-\infty}^{+\infty} \langle f^*(x, z, r, t) f(x + \xi_1, z + \xi_3, s, t + \tau) \rangle e^{-i(k_1\xi_1 + k_3\xi_3 + \omega\tau)} \mathrm{d}\xi_1 \, \mathrm{d}\xi_3 \, \mathrm{d}\tau. \tag{19}$$

The PSD of the steady-state component of the modal displacement $\phi_{d_j d_j}(\omega)$ relates to the modal force PSD $\phi_{f_j f_j}(\omega)$ as (Eq. (10))

$$\begin{aligned} \phi_{d_j d_j}(\omega) &= |H_j(\omega)|^2 \phi_{f_j f_j}(\omega), \\ H_j(\omega) &= \frac{1}{\left(\omega_j^2 - \omega^2\right) + i2\xi_j\omega_j\omega}, \end{aligned} \tag{20}$$

where $|H_j(\omega)|^2$ is the gain in the response of the jth mode. Further, the modal force $\phi_{f_j f_j}(\omega)$ relates to the wall-pressure wavenumber frequency spectrum $\varphi_{pp}(k_1, k_3, \omega)$ as

$$\phi_{f_j f_j}(\omega) = \iint_{-\infty}^{+\infty} \varphi_{pp}(k_1, k_3, \omega) |S_j(k_1, k_3)|^2 \, \mathrm{dk}_1 \, \mathrm{dk}_3. \tag{21}$$

Relating $\varphi_{pp}(k_1, k_3, \omega)$ to the four-dimensional CSD $\varphi_{ff}(r, s, k_1, k_3, \omega)$ using the Green's function, we obtain

$$\phi_{f_j f_j}(\omega) = \iint_{-\delta}^{+\delta} \iint_{-\infty}^{+\infty} G^*(-\delta, r, k) G(-\delta, s, k) \varphi_{ff}(r, s, k_1, k_3, \omega) |S_j(k_1, k_3)|^2 \, \mathrm{dk}_1 \, \mathrm{dk}_3 \, \mathrm{dr} \, \mathrm{ds}, \tag{22}$$

where $S_j(k_1, k_3) = \iint_{\Gamma_{fs}} \varphi_j(x, -\delta, z) e^{i(k_1 x + k_3 z)} \, \mathrm{dx} \, \mathrm{dz}$ is the Fourier transform of the mode shape, and $|S_j(k_1, k_3)|^2$ is the 'modal shape function' (Hwang and Maidanik, 1990). Next, we relate the plate averaged displacement PSD $\phi_{dd}^a(\omega)$ to the

modal displacement PSD $\phi_{d_j d_j}(\omega)$ as

$$\begin{aligned}\phi^a_{dd}(\omega) &= \frac{1}{A_p}\iint_{\Gamma_{fs}} \phi_{dd}(x,-\delta,z)\,\mathrm{d}x\,\mathrm{d}z,\\ &= \frac{1}{A_p}\iint_{\Gamma_{fs}} \sum_{i=1}^{\infty}\sum_{j=1}^{\infty} \phi_{d_i d_j}(\omega)\varphi_i(x,-\delta,z)\varphi_j(x,-\delta,z)\,\mathrm{d}x\,\mathrm{d}z,\\ &\approx \frac{1}{\rho_s L_y^s A_p}\sum_{j=1}^{\infty}\phi_{d_j d_j}(\omega)\left(\because \iint_{\Gamma_{fs}}\varphi_i(x,-\delta,z)\varphi_j(x,-\delta,z)\,\mathrm{d}x\,\mathrm{d}z \approx \frac{1}{\rho L_y^s}\delta_{ij}\right)\end{aligned} \tag{23}$$

Thus, combining Eqs. (20), (22), and (23), we obtain the required expression

$$\begin{aligned}\Gamma^a(r,s,\omega) \approx \frac{1}{\rho L_y^s A_p}\int_{-\infty}^{+\infty}\int_{-\infty}^{+\infty} G^*(-\delta,r,k)G(-\delta,s,k)\varphi_{ff}(r,s,k_1,k_3,\omega)\\ \left(\sum_{j=1}^{\infty}|S_j(k_1,k_3)|^2|H_j(\omega)|^2\right)\mathrm{d}k_1\,\mathrm{d}k_3.\end{aligned} \tag{24}$$

We investigate the structure of the decorrelated contribution from wall-parallel planes by performing spectral POD of the CSD $\Gamma^a(r,s,\omega)$. We use the following inner product to define the orthonormal relation between the eigenfunctions $\bar{\Phi}_i$ and $\bar{\Phi}_j$ of $\Gamma^a(r,s,\omega)$,

$$\int_{-\delta}^{+\delta}\left(\left(-(1-\beta)\frac{\partial^2}{\partial y^2}+\beta\right)\bar{\Phi}_i\right)\bar{\Phi}_j^*\,\mathrm{d}y = \delta_{ij}, \tag{25}$$

where β is a real number satisfying $0 < \beta \leq 1$ and δ_{ij} is the Kronecker delta. Further, the eigenfunctions $\bar{\Phi}_i(r,\omega)$ are assumed to satisfy the zero-Neumann boundary conditions at the wall $r = -\delta$ and $r = +\delta$. Following Anantharamu and Mahesh (2020), we call the above inner product as the Poisson inner product because the symmetric positive definite kernel $\left(-(1-\beta)\frac{\partial^2}{\partial y^2}+\beta\right)$ relates to the Poisson equation. The spectral POD of $\Gamma^a(r,s,\omega)$ is then

$$\Gamma^a(r,s,\omega) = \sum_{j=1}^{\infty}\lambda_j(\omega)\Phi_j(r,\omega)\Phi_j^*(s,\omega), \tag{26}$$

where $\{\Phi_j,\lambda_j\}_{j=1}^{\infty}$ is the set of spectral POD modes and eigenvalues. The spectral POD mode Φ_j relates to the eigenfunction $\bar{\Phi}_j$ of $\Gamma^a(r,s,\omega)$ through the relation $\Phi_j = \left(-(1-\beta)\frac{\partial^2}{\partial y^2}+\beta\right)\bar{\Phi}_j$. The associated eigenvalue problem for $\bar{\Phi}_j$ and λ_j is

$$\int_{-\delta}^{+\delta}\Gamma^a(r,s,\omega)\,\bar{\Phi}_j(s,\omega)\,\mathrm{d}s = \lambda_j(\omega)\left(\left(-(1-\beta)\frac{\partial^2}{\partial y^2}+\beta\right)\bar{\Phi}_j\right)(r,\omega). \tag{27}$$

Further, the functions $\{\Phi_j\}_{j=1}^{\infty}$ and $\{\bar{\Phi}_j\}_{j=1}^{\infty}$ satisfy the orthonormality relation

$$\int_{-\delta}^{+\delta}\Phi_i(y,\omega)\bar{\Phi}_j^*(y,\omega),\mathrm{d}y = \delta_{ij}. \tag{28}$$

The obtained spectral POD eigenvalues gives ranked contribution from each spectral POD mode to the following double integral,

$$\int_{-\delta}^{+\delta}\int_{-\delta}^{+\delta}\frac{G\left(r,s,\frac{\beta}{1-\beta}\right)}{1-\beta}\Gamma^a(r,s,\omega)\,\mathrm{d}r\,\mathrm{d}s = \sum_{j=1}^{\infty}\lambda_j(\omega) \tag{29}$$

where $G(r,s,\beta/(1-\beta))$ is the Green's function given by Eq. (12). For small values of β, the function $G(r,s,\beta/(1-\beta))$ becomes flatter and approaches a constant in r and s, and the left hand side $\int_{-\delta}^{+\delta}\int_{-\delta}^{+\delta}\frac{G\left(r,s,\frac{\beta}{1-\beta}\right)}{1-\beta}\Gamma^a(r,s,\omega)\,\mathrm{d}r\,\mathrm{d}s$ becomes a good proxy for the plate averaged displacement PSD $\phi^a_{dd}(\omega) = \int_{-\delta}^{+\delta}\int_{-\delta}^{+\delta}\Gamma^a(r,s,\omega)\,\mathrm{d}r\,\mathrm{d}s$. Therefore, the obtained spectral POD modes isolate the dominant contributors to plate averaged displacement PSD. For more details about the effectiveness of the Poisson inner product, we refer the reader to Anantharamu and Mahesh (2020).

To obtain the contribution of each spectral POD mode to the plate averaged displacement PSD, we doubly integrate Eq. (26) to obtain

$$\begin{aligned} \phi^a_{dd}(\omega) &= \sum_{j=1}^{\infty} \gamma_j(\omega), \\ \gamma_j(\omega) &= \lambda_j(\omega) \left| \int_{-\delta}^{+\delta} \Phi_j(y,\omega)\, \mathrm{d}y \right|^2;\ j = 1, \ldots, \infty, \end{aligned} \tag{30}$$

where $\gamma_j(\omega)$ is the contribution of jth mode to PSD at frequency ω. Further, we can show that

$$\left| \int_{-\delta}^{+\delta} \Phi_j(y,\omega)\, \mathrm{d}y \right| = \int_{-\delta}^{+\delta} |\Phi_j(y,\omega)| cos\left(\angle \Phi_j(y,\omega) - \angle \Phi_i^n(\omega) \right)\, \mathrm{d}y, \tag{31}$$

where $\angle \cdot$ is the argument of $\cdot$, and $\angle \Phi_j^n(\omega)$ is the argument of the integral $\int_{-\delta}^{+\delta} \Phi_j(y,\omega)\, \mathrm{d}y$. Using Eq. (31) in Eq. (30), we obtain

$$\gamma_j(\omega) = \lambda_j(\omega) \left(\int_{-\delta}^{+\delta} |\Phi_j(y,\omega)| cos\left(\angle \Phi_j(y,\omega) - \angle \Phi_i^n(\omega) \right)\, \mathrm{d}y \right)^2;\ j = 1, \ldots, \infty. \tag{32}$$

From the above equation, we observe that the eigenvalue, and both magnitude and phase of the spectral POD mode all play a role in determining its contribution to the plate averaged displacement PSD. The contribution from different wall-normal locations can constructively or destructively interfere based on the phase of the spectral POD mode. Constructive interference occurs between the contribution from regions where the phase angle satisfies $|\angle \Phi_j(y,\omega) - \angle \Phi_j^n(\omega)| < \pi/2$. Further, the contribution from regions with the phase angle in the range $|\angle \Phi_j(y,\omega) - \angle \Phi_j^n(\omega)| < \pi/2$ destructively interfere with the regions where $\pi/2 < |\angle \Phi_j(y,\omega) - \angle \Phi_j^n(\omega)| < \pi$.

To obtain the contribution of each spectral POD mode to the integrated energy of the net displacement source, we set $s = r$ in Eq. (26) and integrate along r,

$$\begin{aligned} \int_{-\delta}^{+\delta} \Gamma^a(r,r,\omega)\, \mathrm{d}r &= \sum_{j=1}^{\infty} \bar{\lambda}_i(\omega); \\ \bar{\lambda}_i(\omega) &= \lambda_i(\omega) \int_{-\delta}^{+\delta} |\Phi_i(r,\omega)|^2\, \mathrm{d}r, \end{aligned} \tag{33}$$

where $\bar{\lambda}_i$ is the contribution of the ith spectral POD mode to the integrated net displacement source PSD. Further, we can show that if we require the modes to be orthogonal in the L^2 inner product ($\beta = 1$), then $\lambda_i(\omega) = \bar{\lambda}_i(\omega)$. In other words, the modes optimally decompose the integrated PSD as

$$\int_{-\delta}^{+\delta} \Gamma^a(r,r,\omega)\, \mathrm{d}r = \sum_{j=1}^{\infty} \lambda_i(\omega). \tag{34}$$

3.2. Implementation

To compute the net displacement source CSD Γ^a, we need to store the four-dimensional CSD φ_{ff} from the fluid DNS (Eq. (24)). However, storing this function is prohibitively memory intensive. For the $Re_\tau = 400$ case, assuming 2000 frequencies, approximately 1000 TB is required to store the four-dimensional function. To circumvent this issue, we use a parallel, streaming methodology presented in Anantharamu and Mahesh (2020) with a small modification. Anantharamu and Mahesh (2020) presented the implementation to compute the CSD $\Gamma(r,s,\omega) = \int\int_{-\infty}^{+\infty} G^*(-\delta,r,k) G(-\delta,s,k) \varphi_{ff}(r,s,k_1,k_3,\omega)\, \mathrm{d}k_1\, \mathrm{d}k_3$. We modified their implementation to compute the CSD Γ^a given by Eq. (24) instead.

We use the first 50 modes of the plate to perform the summation in Eq. (24). The first 50 modes are sufficient to analyze the plate excitation sources with frequencies smaller than $\omega\delta/u_\tau = 500$. To verify this, we compare the plate averaged displacement spectrum computed using the CSD to that obtained from the one-way coupled DNS. The two spectra match for frequencies smaller than $\omega\delta/u_\tau = 500$ which shows that 50 modes are sufficient (see Fig. 19 in Appendix C). For a discussion on how to choose the number of modes for other Reynolds numbers, and material properties, we refer the reader to Appendix C.

We use the pressure fluctuation Poisson source terms sampled at a resolution of $\Delta t u_\tau/\delta = 3.5 \times 10^{-3}$ for both Reynolds numbers. This amounts to sampling the data once every 7 timesteps of the DNS simulation. In total, we use $20\delta/u_\tau$ and $23\delta/u_\tau$ time units of the simulation data for $Re_\tau = 180$, and $Re_\tau = 400$, respectively. In each FFT chunk, we use 2000 samples which leads to a frequency resolution of $\Delta\omega\delta/u_\tau = 2\pi/7$. To reduce the spectral leakage and to increase the statistical convergence, we use Hanning window with 75% overlap. Further, to account for the reduction in the spectral level after windowing, we multiply the estimated CSD by a factor of 8/3 (Bendat and Piersol, 2011).

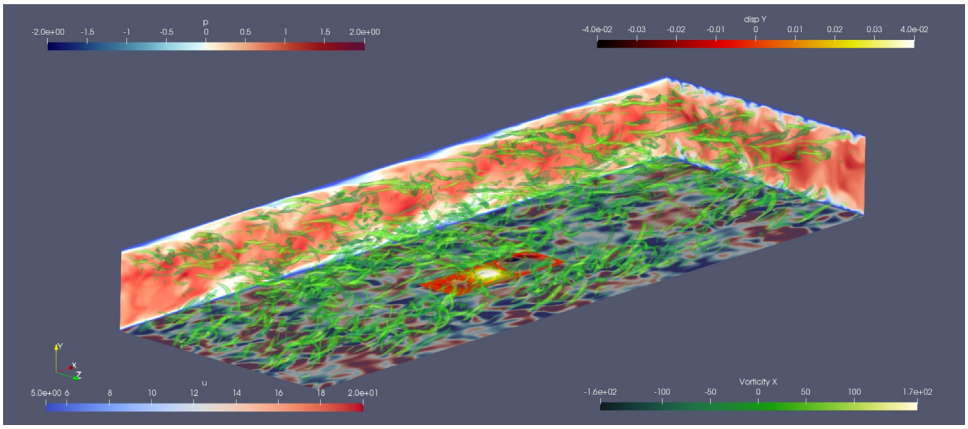

Fig. 2. Instantaneous visualization of the FSI simulation for $Re_\tau = 180$.

Table 4
Plate averaged Root Mean Square (RMS) displacement and velocity of the plate.

Re_τ	$\langle d^{+2} \rangle^{1/2}$	$\langle v^{+2} \rangle^{1/2}$
180	1.81×10^{-2}	5.32×10^{-3}
400	5.32×10^{-2}	7.87×10^{-3}

Table 5
First ten natural frequencies of the plate.

Mode index, j	1	2	3	4	5	6	7	8	9	10
Natural frequency, $\omega_j \delta/u_\tau$	45.05	50.2	59.66	73.9	93.03	116.95	121.65	127.24	136.77	145.55

4. Results and discussion

4.1. FSI simulation results

Fig. 2 shows an instantaneous visualization of the FSI simulation. The vertical and horizontal slices show the fluid streamwise velocity and wall-pressure fluctuations, respectively. The center patch denotes the deformed plate. The isosurfaces are of Q-criterion at non-dimensional values of 500 and 1000. The colored overlayed on the isosurface denotes the streamwise component of vorticity. We use different colormaps for each quantity. The instantaneous field clearly shows the fine scales features of wall turbulence.

The plate averaged root mean square (RMS) wall-normal displacement and velocity for both Re_τ is given in Table 4. Since, the RMS displacement and velocity is much lesser than 1 in viscous units, the one-way coupling is justified.

Fig. 3a and b show the plate averaged wall-normal displacement spectra for both Re_τ in outer (normalized with δ and u_τ) and inner units (normalized with δ_ν and u_τ), respectively. We subsample the plate response at a resolution of $\Delta t u_\tau/\delta = 3.5 \times 10^{-3}$. This amounts to storing the data once every seven timesteps. The total time span of the temporal data used to compute the spectra is $15\delta/u_\tau$ for $Re_\tau = 180$ and $15\delta/u_\tau$ for $Re_\tau = 400$. We divide the temporal data into chunks of size $7\delta/u_\tau$ for averaging. This leads to a spectral resolution of $\Delta\omega\delta/u_\tau = 2\pi/7$. To increase convergence and reduce spectral leakage, we use 75% overlap and Hanning window, respectively. We multiply the obtained spectral estimate by a factor of 8/3 to account for the reduction in the spectral level after windowing (Bendat and Piersol, 2011). Finally, to obtain the plate averaged spectrum, we average the estimated spectrum on the top surface of the plate.

Table 5 shows the first 10 natural frequencies ($\omega_j\delta/u_\tau$; $j = 1, \ldots, 10$) of the plate. The natural frequencies coincide in outer units for both Re_τ. This coincidence occurs because we choose the plate properties to be the same in outer units for the two Re_τ. At these natural frequencies, the plate undergoes resonant vibration leading to large structural response. The plate displacement spectrum in Fig. 3a peaks at the natural frequencies ($\omega_j\delta/u_\tau$) of the plate.

The low frequency ($\omega \ll \omega_1$) spectral levels overlap for both Re_τ. This is because (i) the non-dimensional Young's modulus of the plate is the same for both Re_τ and (ii) the low wavenumber and frequency component of the wall-pressure wavenumber-frequency spectrum is approximately the same in outer units for both Re_τ. We can understand this as follows.

Combining Eqs. (20), (21), and (23), we have

$$\phi^a_{dd}(\omega) \approx \frac{1}{\rho_s L^s_y A_p} \sum_{j=1}^{\infty} |H_j(\omega)|^2 \iint_{-\infty}^{+\infty} \varphi_{pp}(k_1, k_3, \omega) |S_j(k_1, k_3)|^2 \, \mathrm{d}k_1 \, \mathrm{d}k_3. \tag{35}$$

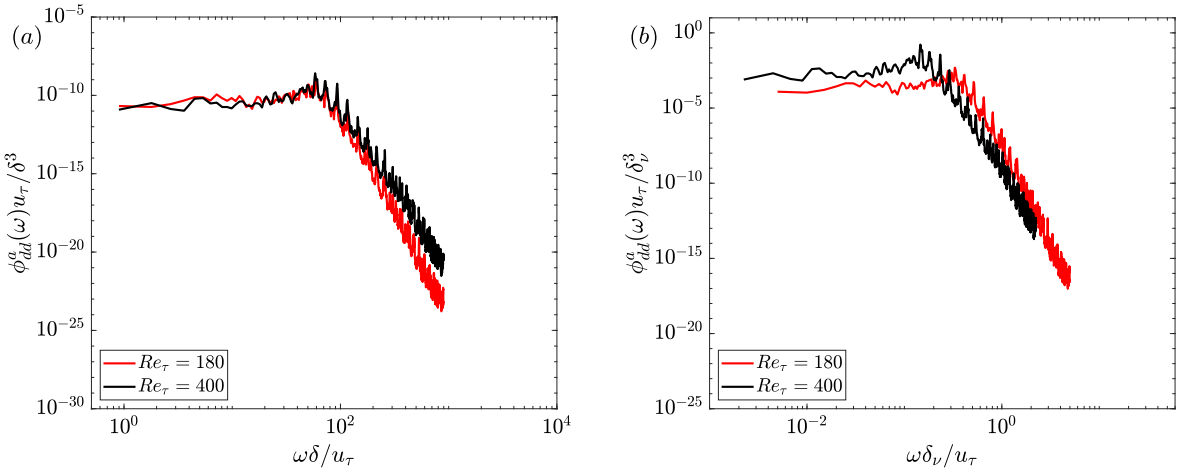

Fig. 3. Plate averaged wall-normal displacement power spectra in (a) outer units (normalized by δ and u_τ) and (b) inner units (normalized by δ_ν and u_τ).

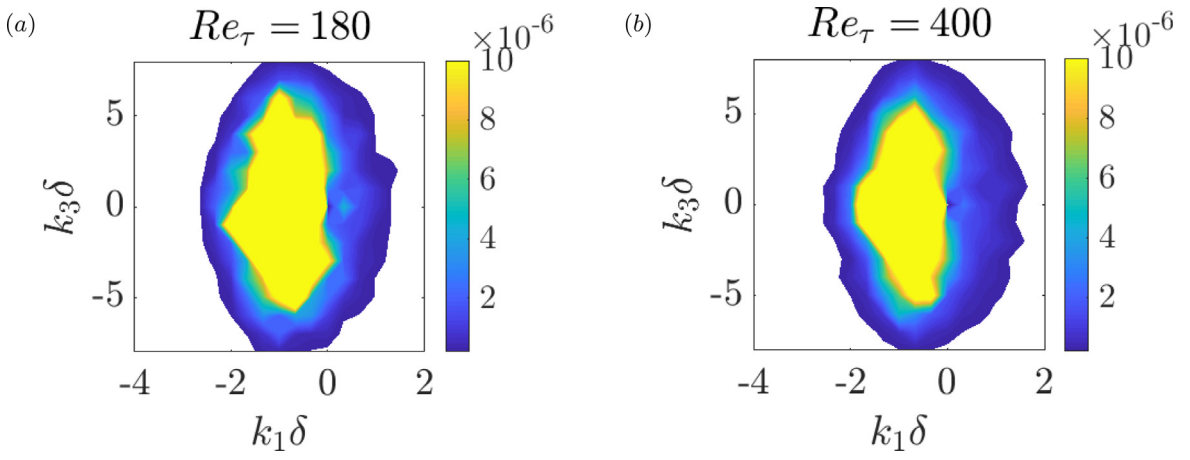

Fig. 4. Product $|S_1(k_1,k_3)|^2\varphi_{pp}(k_1,k_3,\omega = 12.6u_\tau/\delta)$ for (a) $Re_\tau = 180$ and (b) $Re_\tau = 400$. Contours are 100 equally spaced values between 2×10^{-7} and 10^{-5}.

For frequencies $\omega \ll \omega_1$, we can approximate the average spectra using only the first mode as

$$\begin{aligned}\phi^a_{dd}(\omega) &\approx \frac{1}{\rho_s L^s_y A_p}|H_1(\omega)|^2 \iint_{-\infty}^{+\infty} \varphi_{pp}(k_1,k_3,\omega)|S_1(k_1,k_3)|^2\,\mathrm{d}k_1\,\mathrm{d}k_3,\\ &\approx \frac{1}{\rho_s L^s_y A_p \omega_1^4} \iint_{-\infty}^{+\infty} \varphi_{pp}(k_1,k_3,\omega)|S_1(k_1,k_3)|^2\,\mathrm{d}k_1\,\mathrm{d}k_3.\end{aligned} \tag{36}$$

Since, the first natural frequency (ω_1) is proportional to the longitudinal wave speed (c_l) of the plate, we have

$$c_l^4\phi^a_{dd}(\omega) \propto \iint_{-\infty}^{+\infty} \varphi_{pp}(k_1,k_3,\omega)|S_1(k_1,k_3)|^2\,\mathrm{d}k_1\,\mathrm{d}k_3. \tag{37}$$

Note that we have absorbed ρ_s, L^s_y, A_p into the proportionality constant. Non-dimensionalizing the above equation, we have

$$\left(\frac{c_l^4}{u_\tau^3}\right)\frac{\phi^a_{dd}(\omega)}{\delta^3} \approx C\left(\frac{\omega\delta}{u_\tau}, Re_\tau\right), \tag{38}$$

where C is some function of $\omega\delta/u_\tau$ and Re_τ only. We absorb the proportionality constant into C. Fig. 4a and b show the product $|S_1(k_1,k_3)|^2\varphi_{pp}(k_1,k_3,\omega)$ for $Re_\tau = 180$ and 400 in outer units, respectively for a typical frequency $\omega\delta/u_\tau = 12.6 \ll \omega_1$. Overall, the contours are similar for both Re_τ. This similarity of contours occurs in the frequency range $\omega \ll \omega_1$.

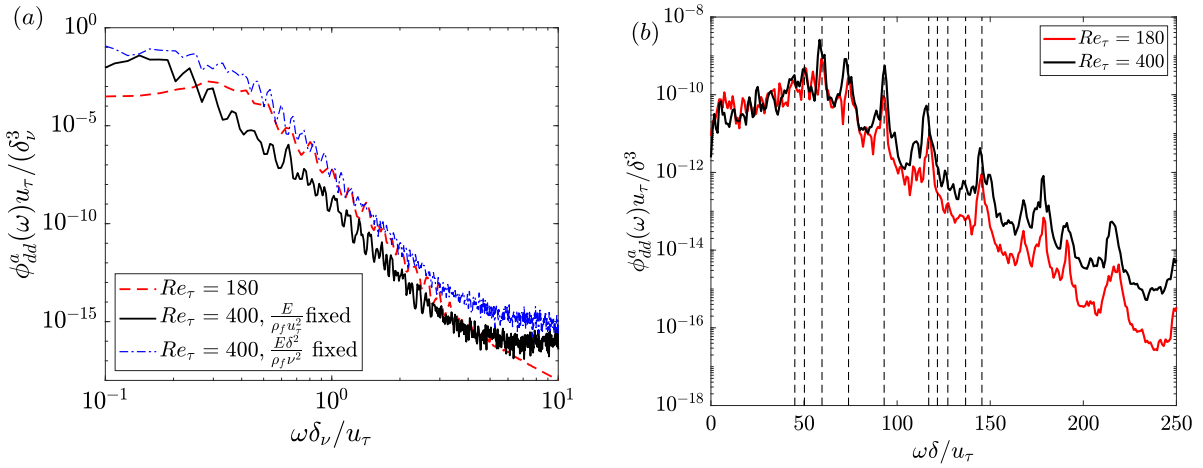

Fig. 5. a) High frequency plate averaged displacement spectra comparison by fixing $E\delta^2/(\rho_f \nu_f^2)$ and $E/\rho_f u_\tau^2$ between the two Reynolds numbers. b) Low frequency plate averaged displacement spectrum in semilogarithmic coordinates. The results are normalized in outer units. The vertical dashed lines denote the frequency coordinates of the first ten natural frequencies in outer units.

Thus, the dependency on Re_τ can be dropped, and we have

$$\left(\frac{c_l^4}{u_\tau^3}\right)\frac{\phi^a_{dd}(\omega)}{\delta^3} \approx C\left(\frac{\omega\delta}{u_\tau}\right). \tag{39}$$

Further, substituting for c_l in terms of the Young's modulus E, we have

$$\left(\frac{E}{\rho_s u_\tau^2}\right)^2\frac{\phi^a_{dd}(\omega)u_\tau}{\delta^3} \approx C\left(\frac{\omega\delta}{u_\tau}\right). \tag{40}$$

Since, $\frac{E}{\rho_s u_\tau^2}$ is the same for both Re_τ, we have the required result,

$$\frac{\phi^a_{dd}(\omega)u_\tau}{\delta^3} \approx C\left(\frac{\omega\delta}{u_\tau}\right). \tag{41}$$

Fig. 3b shows the plate averaged displacement PSD with inner scaling ($\delta_\nu = \nu_f/u_\tau$ and u_τ as length and velocity scale, respectively). The PSD at the two Re_τ do not overlap in the high-frequency region. This is because for identical natural frequencies in inner units, the corresponding modal wavenumbers do not match in inner units, i.e., if j and k are two mode indices such that

$$\left(\omega_j\delta_\nu/u_\tau\right)_{Re_\tau=180} = \left(\omega_k\delta_\nu/u_\tau\right)_{Re_\tau=400}, \tag{42}$$

then

$$\left(k_{m,j}\delta_\nu\right)_{Re_\tau=180} \neq \left(k_{m,k}\delta_\nu\right)_{Re_\tau=400}. \tag{43}$$

Therefore, the plate filters different wavenumbers from the wall-pressure wavenumber frequency spectrum in viscous units leading to dissimilar high-frequency spectral levels.

A better overlap of high-frequency spectral levels is observed (shown in Fig. 5a) if $E\delta^2/\left(\rho_f \nu_f^2\right)$ (velocity scale is ν_f/δ) is fixed for the two Reynolds numbers instead of $E/\rho_f u_\tau^2$ (velocity scale is u_τ). This is because for fixed $E\delta^2/\left(\rho_f \nu_f^2\right)$ and coinciding natural frequencies in inner units, the corresponding modal wavenumbers also coincide in inner units. We explain this as follows. Let j and k be the mode indices with coinciding natural frequencies in inner units for $Re_\tau = 180$ and 400, respectively, i.e.,

$$\left(\omega_j\delta_\nu/u_\tau\right)_{Re_\tau=180} \approx \left(\omega_k\delta_\nu/u_\tau\right)_{Re_\tau=400}. \tag{44}$$

We can show that for fixed $E\delta^2/\left(\rho_f \nu_f^2\right)$ and L_y^s/δ, we have

$$\left(k_{m,j}\delta\right)^2 \approx \left(k_{m,k}\delta\right)^2\left(\frac{180}{400}\right)^2. \tag{45}$$

Further, non-dimensionalizing in viscous units, we obtain the desired relation,

$$\left(k_{m,j}\delta_\nu\right)_{Re_\tau=180} \approx \left(k_{m,k}\delta_\nu\right)_{Re_\tau=400} \tag{46}$$

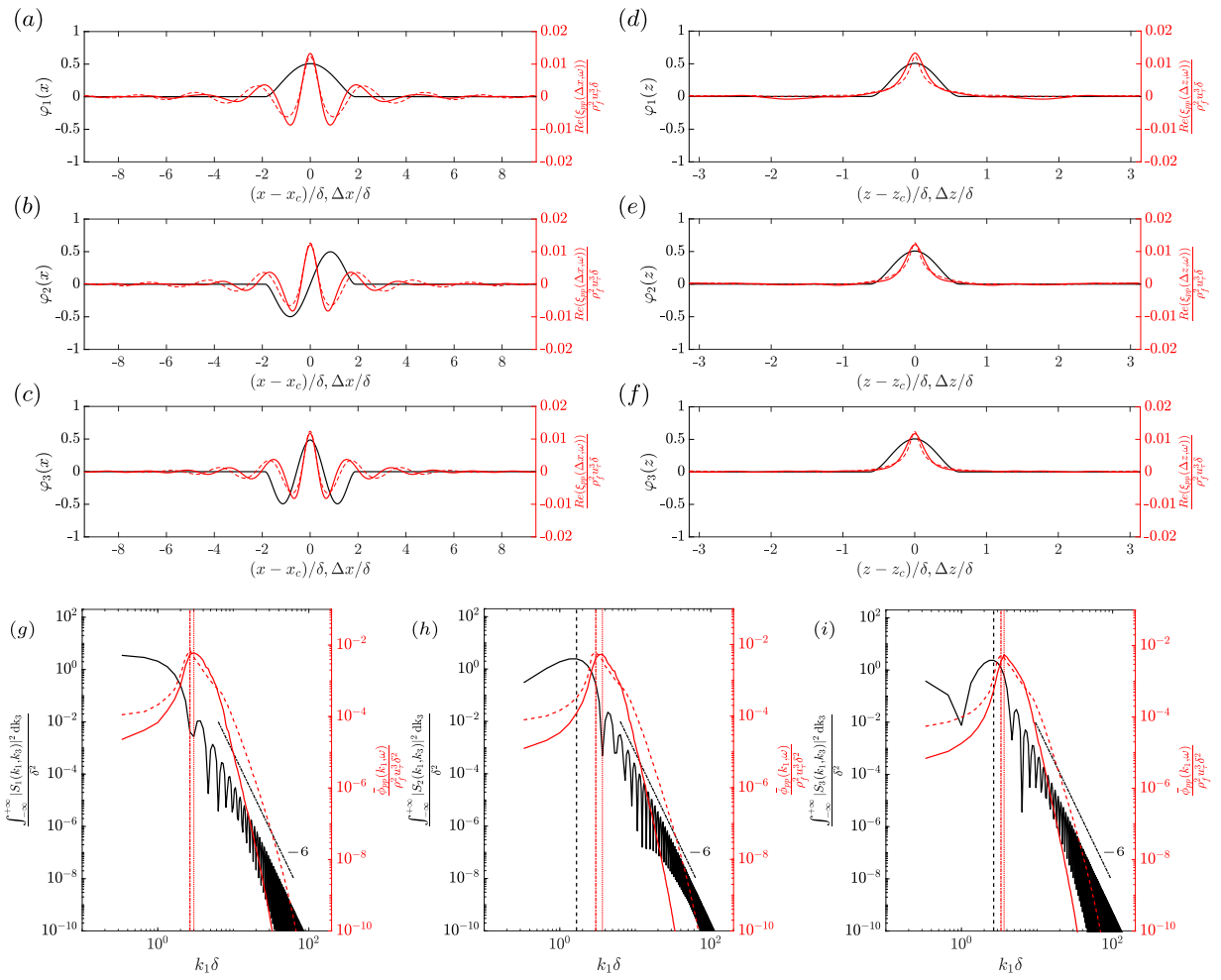

Fig. 6. Comparison of the streamwise length scales of the wall-pressure and the plate deflection for the first three natural frequencies. Figures (a), (b), and (c) compare the streamwise shape $\varphi_j(x)$; $j = 1, 2, 3$ of the first three modes to the real part of the streamwise CSD of the DNS wall-pressure fluctuations $\xi_{pp}(\Delta x, \omega)$ at its natural frequencies. Here, Δx is the streamwise separation distance. Black solid line denotes the shape of the plate mode along the streamwise direction. Red solid and dashed lines denote the real part of the streamwise CSD for $Re_\tau = 180$ and 400, respectively. x_c is the streamwise coordinate of the center of the domain. Figures (d), (e), and (f) are the spanwise counterparts of figures (a), (b) and (c), respectively. $\varphi_j(z)$; $j = 1, 2, 3$ denote the spanwise shape of the first three modes, and $\xi_{pp}(\Delta z, \omega)$ denotes the spanwise CSD of the DNS wall-pressure fluctuations. Figures (g), (h) and (i) compare the integrated modal shape function $\int_{-\infty}^{+\infty} |S_j(k_1, k_3)|^2 \, \mathrm{d}k_3$ to the streamwise wavenumber frequency spectrum $\bar{\phi}_{pp}(k_1, \omega) = \int_{-\infty}^{+\infty} \varphi_{pp}(k_1, k_3, \omega) \mathrm{d}k_3$ of the DNS wall-pressure fluctuations as a function of the streamwise wavenumber k_1. Figures (a), (d), and (g) are for mode 1. Figures (b), (e), and (h) are for mode 2. Figures (c), (f) and (i) are for mode 3.

4.2. Length scale comparison for the first three modes

Fig. 5b provides a closer look at the resonant vibration levels for the first few modes in semi-logarithmic coordinates. In the same figure, we also mark the frequency ordinate of the first ten natural frequencies of the plate using vertical black dashed lines. The resonant spectrum level at the first natural frequency is lower than at the second mode. The global maximum of the spectrum occurs at the third natural frequency. This behavior is due to the relative ratio of the streamwise length scales of the structural mode and the pressure fluctuation correlations at the mode's natural frequency. The lower resonant vibration at the first mode is because the relative ratio is large. And, the maximum resonant vibration at the third mode is because the relative ratio is close to unity indicating similar fluid and solid length scales.

We further investigate this in Fig. 6a where we compare the streamwise length scales of the fluid and solid for the plate's first mode. For the structural length scale, we use the solid black line to plot the plate's first mode shape in the streamwise direction. Note that the mode shape is the same for both Re_τ. For the fluid length scale, we use the solid and dashed red lines to plot the real part of the streamwise CSD of the DNS wall-pressure fluctuations at the mode's natural frequency. The solid red line is for $Re_\tau = 180$, and the dashed red line is for $Re_\tau = 400$. The streamwise CSD shows the correlation of the fluid wall-pressure fluctuations at the mode's natural frequency. The comparison shows that

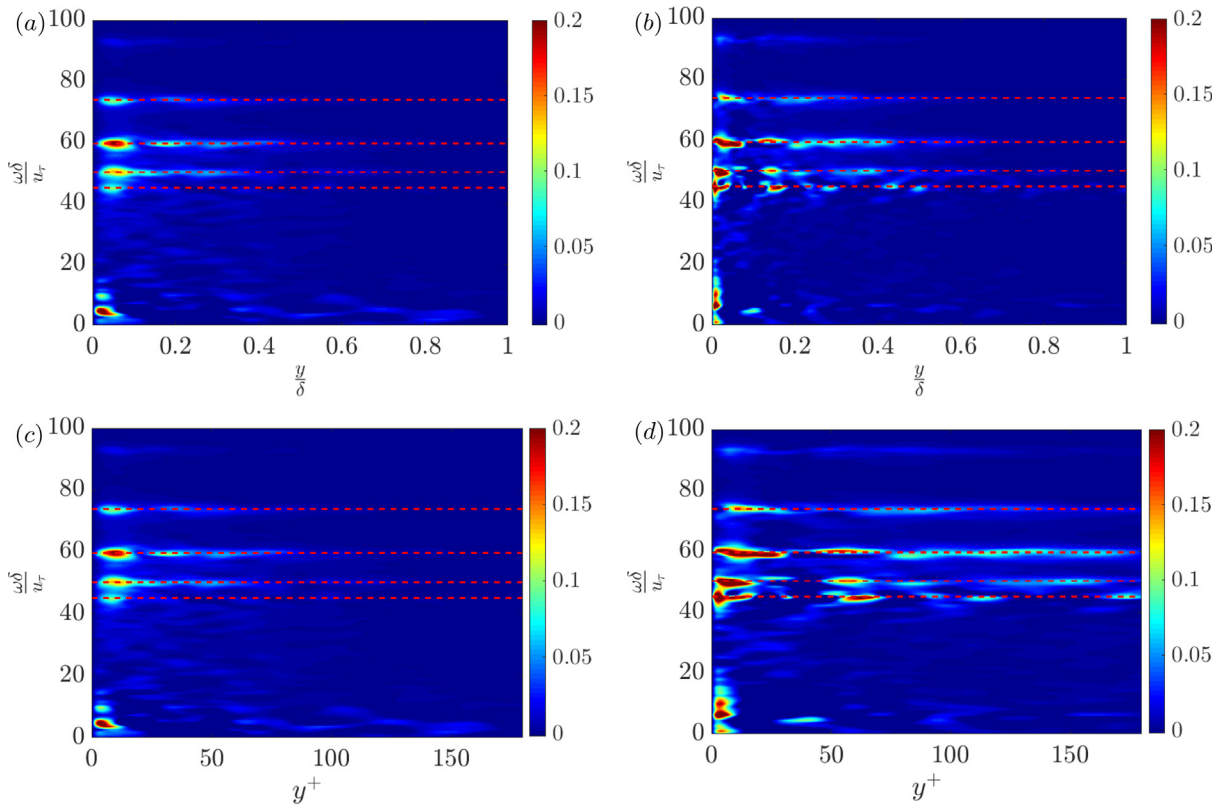

Fig. 7. Real part of the normalized wall displacement–net displacement source CSD $\frac{Re(\Psi_a(y,\omega))}{\int_{-\infty}^{+\infty}\int_{-1}^{+1}\Psi_a(y,\omega\delta)\,dy/\delta\,d\omega\delta/u_\tau}$. The wall-normal distance is in outer units in figures (a) and (b), and is in inner units in figures (c) and (d). Figures (a) and (c) are for $Re_\tau = 180$, and figures (b) and (d) are for $Re_\tau = 400$. In all the figures, the contours are 100 equally spaced values between −0.002 and 0.2. Horizontal dashed red lines denote the first four natural frequencies of the plate. (For interpretation of the references to color in this figure legend, the reader is referred to the web version of this article.)

the streamwise length scale of the wall-pressure is much finer than the plate's mode shape. This difference leads to less forcing on the first mode by the wall-pressure fluctuations and therefore, smaller resonant vibration.

One can better understand how the difference in the streamwise length scale translates to less modal forcing in wavenumber space (Blake, 2017). In Fig. 6e, we compare the wall-pressure wavenumber frequency spectrum to the modal shape function at the plate's first natural frequency. Both the spectrum and the modal shape functions are integrated along the spanwise wavenumbers, and hence the curves are only a function of the streamwise wavenumber. The product of these two functions reflects the contribution from each streamwise wavenumber to the modal forcing. For an exact expression of this contribution, see the integrand of Eq. (1).

From Fig. 6e, we can observe that the modal shape function peaks at $k_1\delta = 0$, and its values are similar to the peak value until $k_1\delta \approx 1$. However, the wavenumber frequency spectrum peaks at the convective wavenumber $k_1\delta \approx 2.5$. This separation between the dominant fluid and solid wavenumbers results in a smaller product of the two functions, which, in turn leads to smaller modal forcing.

For the above discussion, we considered only the first mode. For higher mode indices 2 and 3, the streamwise structural length scale is smaller than mode 1. Fig. 6b and c compare these higher mode shapes to the fluid wall-pressure streamwise CSD at the corresponding natural frequencies. Fig. 6b is for mode 2, and Fig. 6c is for mode 3. As we go from mode 1 to mode 2, the length scale of both the mode and wall-pressure decrease, but the mode's length scale decreases faster. This decrease continues as we go from mode 2 to mode 3, where the two length scales approach each other. This similarity in the length scales leads to maximum resonant vibration at mode 3.

In the spectral space, this streamwise length scale similarity of the higher modes appears as a coincidence between the modal wavenumber (peak of the modal shape function) and the convective wavenumber (peak of the wall-pressure streamwise wavenumber frequency spectrum). Fig. 6h and i show this comparison in wavenumber space for modes 2 and 3, respectively. Here, we plot the same quantities plotted in Fig. 6g but for the higher modes. The two peaks start to approach each other as we go from mode 1 (Fig. 6g) to mode 2 (Fig. 6h), and move even closer as we go from mode 2 to mode 3 (Fig. 6i). This coincidence leads to relatively higher modal forcing for modes 2 and 3 than mode 1 and is the reason for the higher resonant vibration of the higher modes.

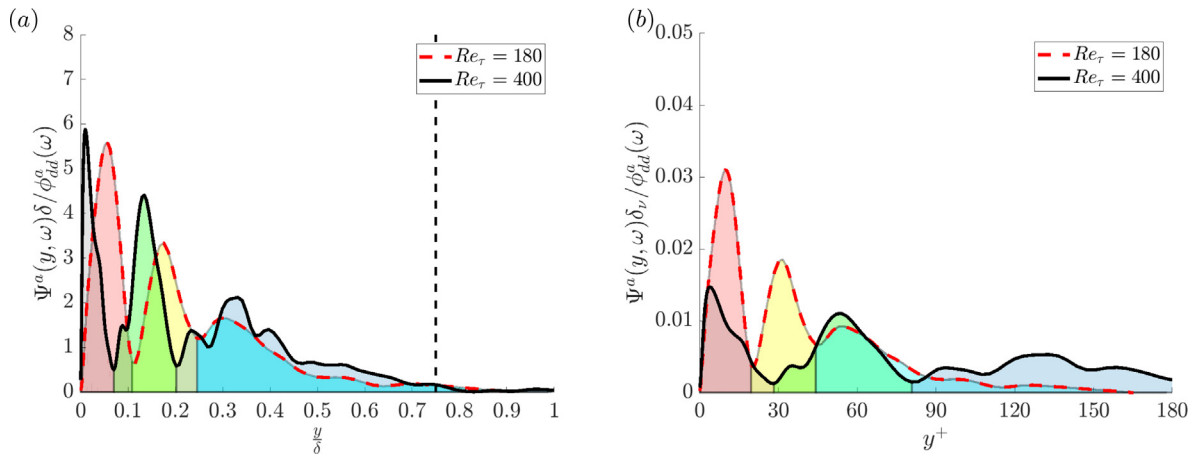

Fig. 8. Fractional plate averaged wall displacement-net displacement source CSD (normalized by the spectrum) at the third natural frequency for $Re_\tau = 180$ and 400. Figure (a) is in outer units and figure (b) is in inner units. Vertical dashed line in figure (a) denotes $y/\delta = 0.75$.

Table 6
Fractional contribution of different wall-normal regions to the plate averaged displacement spectrum at the second, third and fourth natural frequency.

Range	2nd mode		3rd mode		4th mode	
	$Re_\tau = 180$	$Re_\tau = 400$	$Re_\tau = 180$	$Re_\tau = 400$	$Re_\tau = 180$	$Re_\tau = 400$
$0 < y^+ < 30$	0.51	0.29	0.50	0.21	0.53	0.29
$30 < y^+ < 0.2Re_\tau$	0.07	0.24	0.10	0.31	0.08	0.24
$0.2 < y/\delta < 1$	0.42	0.46	0.40	0.48	0.39	0.47

For the current example, the spanwise length scales of the first three modes are comparable to that of the wall-pressure fluctuations. Fig. 6d–f show this comparison. For the spanwise solid length scale, we plot the spanwise shape of the mode. For the fluid length scale, we plot to the spanwise wall-pressure CSD at the mode's natural frequencies. These figures are the spanwise counterparts of Fig. 6a–c. The modes in Fig. 6d–f are identical to each other. This is because for the current aspect ratio (length/width) of the plate, as we go from mode 1 to 3, the streamwise mode index grows while the spanwise mode index stays the same. The corresponding fluid length scales are comparable to the structural length scale and decrease slightly with increasing natural frequency.

4.3. Wall-normal distribution of fluid sources

Fig. 7 shows the plate-averaged wall displacement–net displacement source CSD $\Psi^a(y,\omega)$ normalized by its double integral. In Figs. 7a and b, the wall-normal distance is in outer units. In Fig. 7c and d, the wall-normal distance is in inner units. Fig. 7a and c are for $Re_\tau = 180$, and Fig. 7b and d are for $Re_\tau = 400$. In all figures, the frequency ordinates of the four horizontal dashed red lines are the first four natural frequencies of the plate (Table 5). Recall, from Eq. (18), integrating the CSD $\Psi^a(y,\omega)$ along y gives the plate averaged displacement spectrum. Therefore, the contours reflect the contribution of different wall-parallel planes to the displacement PSD as a function of frequency. Specifically, they indicate the contribution from the correlations between the fluid sources at a given distance from the wall and every other plane. From a visual inspection of the contours in Fig. 7, we see that the fluid sources around the natural frequencies are the dominant contributors to the structural response. This dominant contribution peaks close to the wall (Fig. 7c and d). The dominant contribution's width extends well up to the outer region of the channel (Fig. 7c and d).

In the previous section, we saw that the resonant vibration reaches its maximum for the third mode. We now investigate the wall-normal distribution of the fluid sources that contribute to this resonant vibration. We do so by analyzing the CSD $\Psi^a(y,\omega)$ at its natural frequency in Fig. 8. We normalize the curves so that they integrate to unity along the wall-normal direction. In Fig. 8a, the wall-normal distance is in outer units. In Fig. 8b, the wall-normal distance is in inner units. We use a dashed red line for $Re_\tau = 180$, and solid black line for $Re_\tau = 400$.

The global maximum of the CSD occurs in the inner region of the channel and the sources extend up to $y/\delta = 0.75$. In addition to this near-wall peak, we observe two other peak regions. We argue that these three peaks regions indicate the contribution of the fluid sources in the channel's inner, overlap, and outer regions. The peak region close to the wall, shaded in red for $Re_\tau = 180$ and in black for $Re_\tau = 400$, extends to $y^+ \approx 22$ and 28, respectively. This region indicates the contribution of the inner-layer sources because its upper bound scales better in inner-units and is lesser than $y^+ = 30$ (the channel's inner region bound). The second peak region, shaded in yellow for $Re_\tau = 180$ and green for $Re_\tau = 400$,

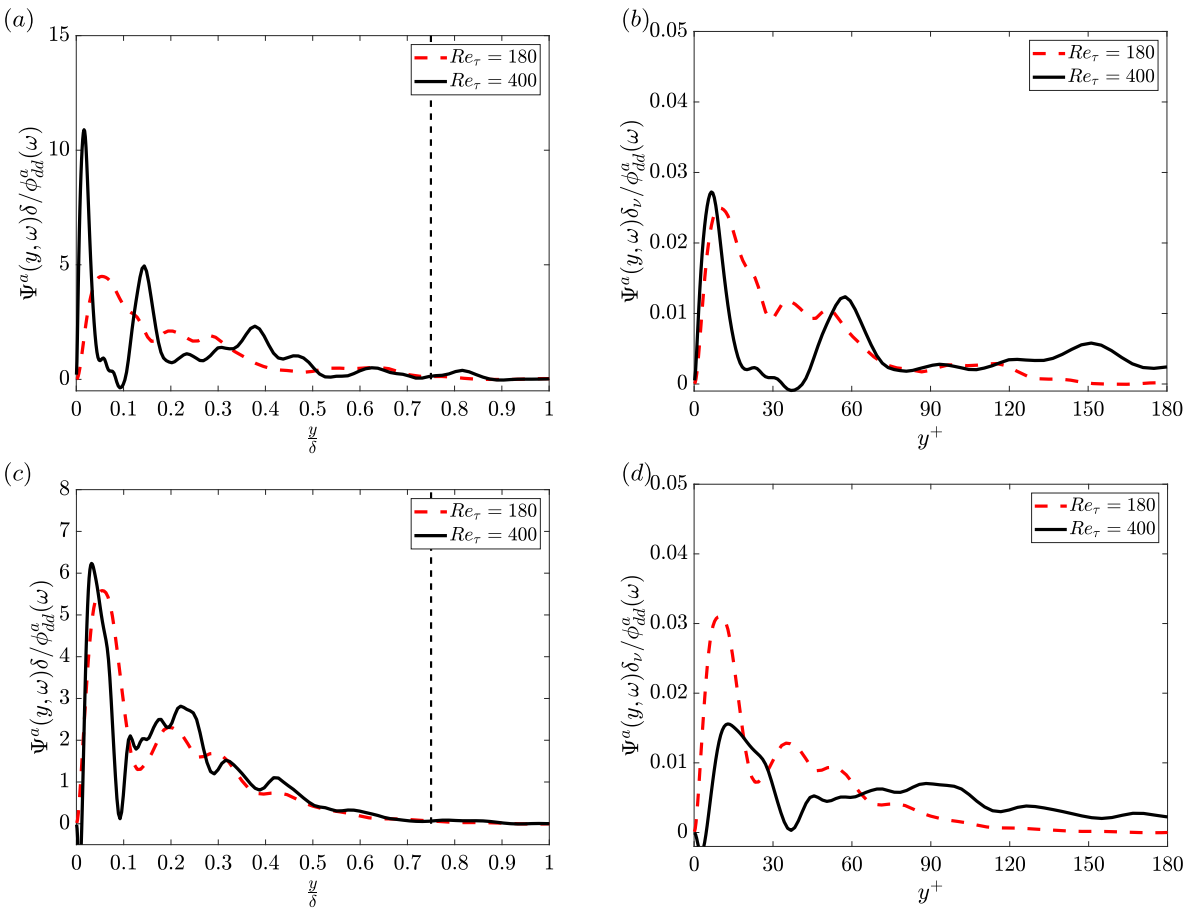

Fig. 9. Fractional plate averaged wall displacement-net displacement source CSD (normalized by the spectrum) at the second and fourth natural frequency for $Re_\tau = 180$ and 400. Figures (a) and (b) are at the second natural frequency and figures (c) and (d) are the fourth natural frequency. Figures (a) and (c) are in outer units and figure (b) and (d) are in inner units. Vertical dashed line in figures (a) and (c) denotes $y/\delta = 0.75$.

Table 7
Fractional contribution of different wall-normal regions to the plate averaged root mean square displacement (accounted by the first 50 modes) for the two Re_τ.

Range	$Re_\tau = 180$	$Re_\tau = 400$
$0 < y^+ < 30$	0.52	0.34
$30 < y^+ < 0.2Re_\tau$	0.06	0.17
$0.2 < y/\delta < 1$	0.41	0.49

extends to $y/\delta = 0.2$ and 0.25, respectively. Note that the lower bound of this region is the upper bound of the previous region. The upper and lower bounds scale better in different units, and therefore, this second peak region denotes the channel's overlap region contribution to the plate excitation. The third peak region is farthest from the wall. It is shaded in cyan for $Re_\tau = 180$ and in dark blue for $Re_\tau = 400$, and extends from $y/\delta = 0.2$ and 0.25, respectively, to the channel centerline. Hence, this region constitutes the contribution of the outer-region sources to the plate excitation.

We compare the fractional contribution of the inner, overlap, and the outer regions to the PSD by integrating the CSD (Fig. 8) from $0 < y^+ < 30$, $30 < y^+ < 0.2Re_\tau$, and $0.2 < y/\delta < 1$, respectively. The second column of Table 6 shows this comparison for the third mode. The values sum to unity for both Re_τ. We observe that, for $Re_\tau = 180$, nearly, 50% of the peak resonant vibration comes from the overlap and outer regions of the channel. For $Re_\tau = 400$, this increases to 80%. If the plate material parameters remain fixed in outer units, we expect this trend to continue for even higher Reynolds numbers.

In the above analysis, we focused only on the maximum resonant vibration at the third mode. In Fig. 9, similar to Fig. 8, we show the fractional CSD at the second and fourth natural frequencies. Fig. 9a and b are for the second mode. Fig. 9c and d are for the fourth mode. In Fig. 9a and c, the wall-normal distance is in outer units and in Fig. 9b and d, they are in inner units. We choose the second and the fourth modes because these two constitute the next largest resonant vibration

after the third mode. The CSDs in Fig. 8 peak in the buffer layer and have reasonable values for $y/\delta < 0.75$. Similar to the third mode, we compute the relative contribution from the inner, overlap and outer regions at the second and fourth natural frequency ny integrating the CSD in each region. Column 1 in Table 6 is for the second mode and column 3 is for the fourth mode. These relative contributions are similar to the previously discussed third mode, and show a similar trend with Reynolds number. Further, we integrate the CSD $\Psi^a(y,\omega)$ in frequency and obtain the contribution of each wall-normal region to the plate-averaged RMS displacement. The resulting values shown in Table 7 are similar to that in Table 6.

Overall, the contribution from the fluid sources to the plate excitation peaks in the buffer region of the channel at the Reynolds numbers considered. However, if we consider the integrated contribution, then the sources in the overlap and the outer region of the channel also have a large relative contribution. This outer and overlap contribution is higher for the higher Reynolds number.

The Mellen form (Corcos, 1964) of the wall-pressure wavenumber frequency spectrum has an interesting implication on the associated one-way coupling. We show that for a Mellen type wavenumber frequency spectrum, the plate averaged displacement PSD and the wall-pressure PSD couple in a similar manner with the channel fluid sources up to a multiplicative constant. The Mellen type wavenumber-frequency spectrum $\varphi_{pp}(k_1,k_3,\omega)$ takes the form,

$$\varphi_{pp}(k_1,k_3,\omega)=\phi_{pp}(\omega)\frac{1}{2\pi}\frac{(\alpha_1\alpha_3)^2}{\left[(\alpha_1\alpha_3)^2+(\alpha_1k_3U_c/\omega)^2+\alpha_3^2\,(1-k_1U_c/\omega)^2\right]^{3/2}} \tag{47}$$

where α_1 and α_3 are the parameters that govern the decay of the spectrum in streamwise and spanwise directions, and U_c is the convection velocity at frequency ω. The wall-pressure PSD $\phi_{pp}(\omega)$ can be expressed as the wall-normal integral (Anantharamu and Mahesh, 2020) using the Green's function formulation,

$$\begin{aligned}\phi_{pp}(\omega)&=\iint_{-\delta}^{+\delta}\Gamma(r,s,\omega)\,\mathrm{d}r\,\mathrm{d}s,\\ \Gamma(r,s,\omega)&=\iint_{-\infty}^{+\infty}G^*(-\delta,r,k)G(-\delta,s,k)\varphi_{ff}(r,s,k_1,k_3,\omega)\,\mathrm{d}k_1\,\mathrm{d}k_3.\end{aligned} \tag{48}$$

where $\Gamma(r,s,\omega)$ is the net wall-pressure source CSD. The net wall-pressure source is a function $f_G(x,y,z,t)$ whose integral in the wall-normal direction gives the instantaneous wall-pressure fluctuation $p(x,-\delta,z,t)=\int_{-\delta}^{+\delta}f_G(x,y,z,t)\,\mathrm{d}y$. Combining Eqs. (20), (21), (23), and (48), we obtain the desired result,

$$\begin{aligned}\phi_{dd}^a(\omega)=&=\iint_{-\delta}^{+\delta}\Gamma^a(r,s,\omega)\,\mathrm{d}r\,\mathrm{d}s=\iint_{-\delta}^{+\delta}\Gamma(r,s,\omega)\alpha(\omega)\,\mathrm{d}r\,\mathrm{d}s,\\ \alpha(\omega)&=\iint_{-\infty}^{+\infty}\frac{(\alpha_1\alpha_3)^2}{\left[(\alpha_1\alpha_3)^2+(\alpha_1k_3U_c/\omega)^2+\alpha_3^2\,(1-k_1U_c/\omega)^2\right]^{3/2}}\\ &\quad\left(\sum_{j=1}^{\infty}\left|\hat{H}_j(\omega)\right|^2|S_j(k_1,k_3)|^2\right)\mathrm{d}k_1\,\mathrm{d}k_3.\end{aligned} \tag{49}$$

Note that $\alpha(\omega)$ is a positive number. Thus, for a Mellen type spectrum both plate averaged displacement PSD and wall-pressure PSD couple in a similar manner with the fluid sources. We choose the Mellen model for the analysis because its isocontours in the wavenumber domain take an elliptic-like shape. The elliptic shape is more physical than the diamond-like isocontours of the Corcos (1964) model. This similarity between the fluid–wall-pressure coupling and the fluid–solid coupling is true for any wavenumber-frequency spectrum that takes a separable form $\varphi_{pp}(k_1,k_3,\omega)=\phi_{pp}(\omega)A\,(k_1U_c/\omega,k_3U_c\omega)$, where $A\,(k_1U_c/\omega,k_3U_c\omega)$ is the similarity function that describes the streamwise and spanwise form of the spectrum.

4.4. Spectral POD of fluid sources

Before we present the spectral POD results of $\Gamma^a(r,s,\omega)$, we discuss the relevance of the spectral POD modes and eigenvalues to the plate surface displacement. Recall Eq. (2) that relates the surface displacement at a point (x,z) on the plate to the net displacement source,

$$d(x,-\delta,z,t)=\int_{-\delta}^{+\delta}f_d(x,y,z,t)\,\mathrm{d}y. \tag{50}$$

The Fourier transform of the net displacement source can be expanded in the spectral POD basis $\{\Phi_j^*\}_{j=1}^{\infty}$ as

$$\begin{aligned}f_d(x,y,z,t)&=\int_{-\infty}^{+\infty}\hat{f}(x,y,z,\omega)e^{i\omega t}\,\mathrm{d}\omega,\\ &=\int_{-\infty}^{+\infty}\sum_{j=1}^{\infty}\alpha_j(x,z,\omega)\Phi_j^*(y,\omega)\,e^{i\omega t}\,\mathrm{d}\omega,\end{aligned} \tag{51}$$

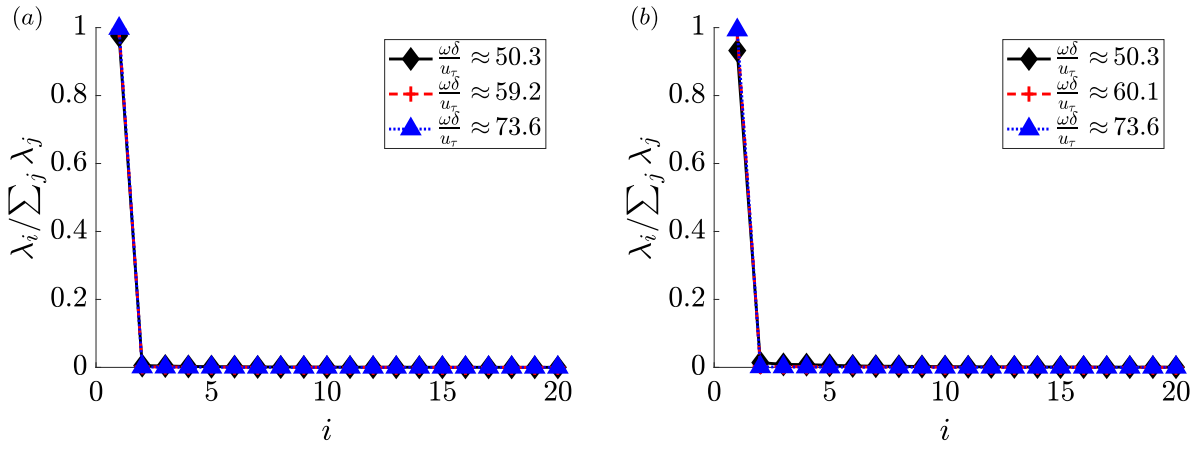

Fig. 10. Spectral POD eigenvalues for (a) $Re_\tau = 180$ and (b) $Re_\tau = 400$ computed using the Poisson inner product ($\beta = 0.01$).

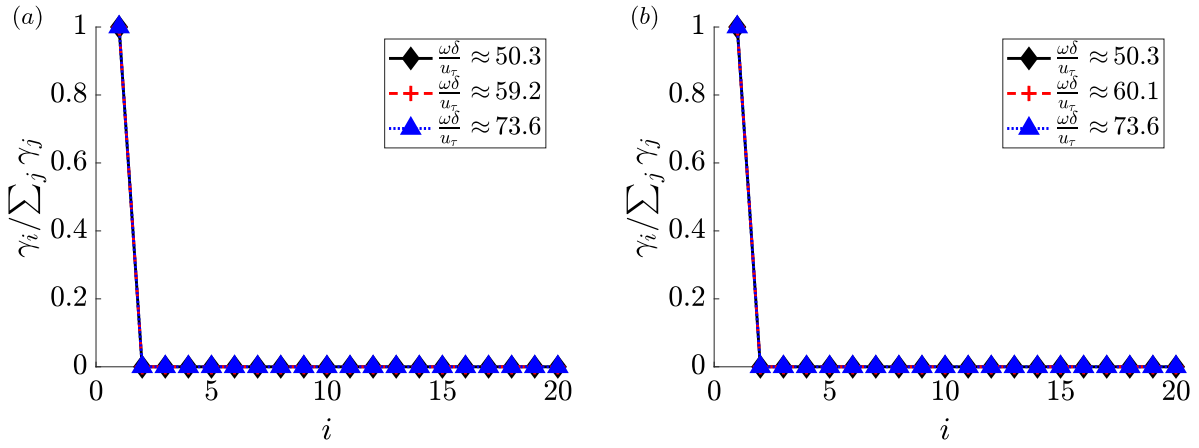

Fig. 11. Contribution of each spectral POD mode to plate averaged displacement PSD for (a) $Re_\tau = 180$ and (b) $Re_\tau = 400$ computed using the Poisson inner product ($\beta = 0.01$).

where $\{\alpha_j(x, z, \omega)\}_{j=1}^{\infty}$ are the coefficients of expansion of $\hat{f}_d(x, y, z, \omega)$. Using Eq. (51) in Eq. (50), and rearranging the integral, we have

$$d(x, -\delta, z, t) = \int_{-\infty}^{+\infty} \alpha_j(x, z, \omega) e^{i\omega t} \left(\int_{-\delta}^{+\delta} \Phi_j^*(y, \omega)\, \mathrm{d}y \right) \mathrm{d}\omega. \tag{52}$$

Using the expression $\Phi_j^*(y, \omega) = |\Phi_j(y, \omega)| e^{-\angle \Phi_j(y,\omega)}$ in the above equation, we have

$$d(x, -\delta, z, t) = \int_{-\infty}^{+\infty} \alpha_j(x, z, \omega) e^{i\omega t} \left(\int_{-\delta}^{+\delta} |\Phi_j(y, \omega)| e^{-\angle \Phi_j(y,\omega)}\, \mathrm{d}y \right) \mathrm{d}\omega. \tag{53}$$

The above equation expresses the plate displacement as sum of contributions from each spectral POD mode. Further, the coefficients $\{\alpha_j(x, z, \omega)\}_{j=1}^{\infty}$ are decorrelated in the plate averaged sense, i.e.,

$$\frac{1}{A_p} \int_{\Gamma_{fs}} \langle \alpha_j(x, z, \omega) \alpha_k(x, z, \omega_o) \rangle \, \mathrm{d}x \, \mathrm{d}z = \lambda_j(\omega) \delta_{jk} \delta(\omega - \omega_o), \tag{54}$$

where δ_{ij} is the Kronecker delta and $\delta(\omega - \omega_o)$ is the Dirac Delta function. We include the effect of structures of all length scales because we integrate over all wavenumbers in Eq. (24).

We set the parameter β in the Poisson inner product (Eq. (25)) to a small value of 0.01 to compute the spectral POD modes and eigenvalues. We did not observe a change in the computed mode shapes and the contribution of the modes to the plate averaged displacement PSD for values smaller than 0.01. Further, we will see that the value $\beta = 0.01$ identifies a single dominant mode of the net displacement source responsible for the plate excitation. For more details on the effect

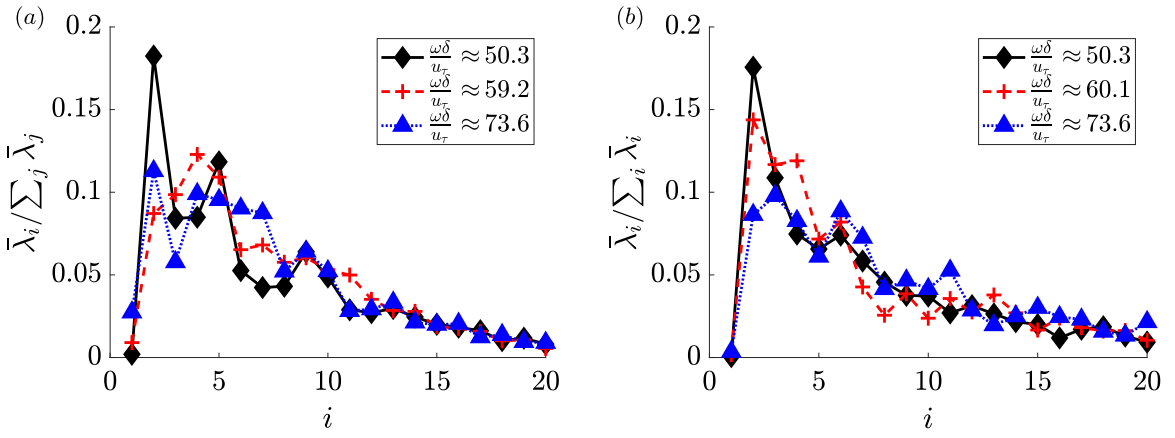

Fig. 12. Contribution of each spectral POD mode computed using the Poisson inner product ($\beta = 0.01$) to the net displacement source PSD for (a) $Re_\tau = 180$ and (b) $Re_\tau = 400$. For definition of $\bar{\lambda}_i$, see Eq. (33).

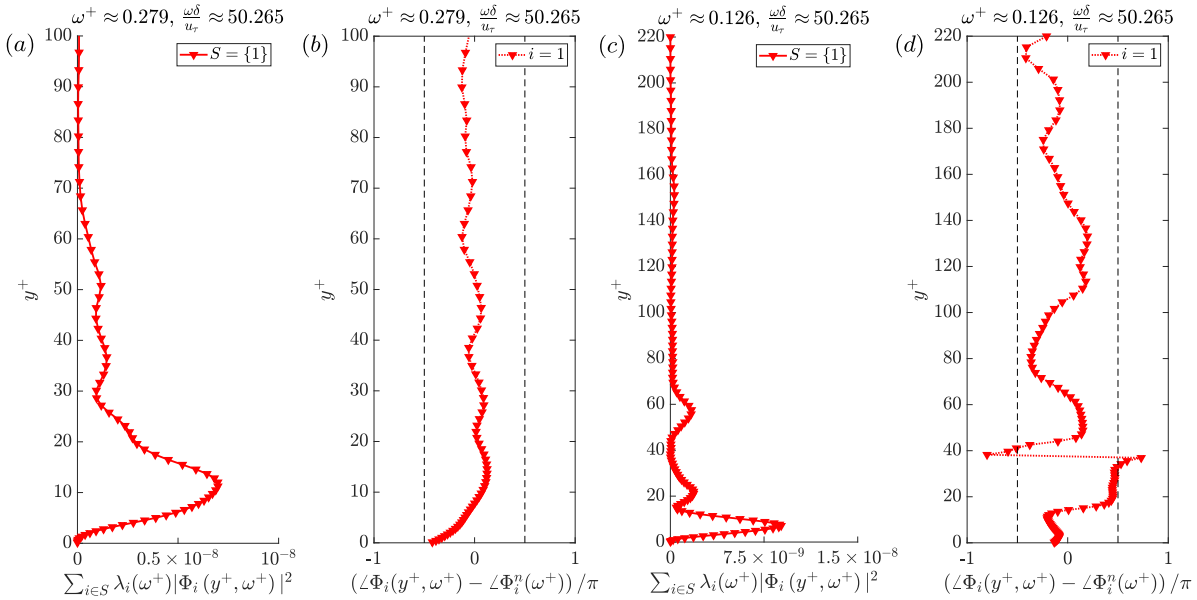

Fig. 13. Envelope and phase of the dominant spectral POD mode computed using the Poisson inner product ($\beta = 0.01$) for $Re_\tau = 180$ ((a)-envelope, (b)-phase) and $Re_\tau = 400$ ((c)-envelope, (d)-phase) at peak frequency $\omega\delta/u_\tau \approx 50.2$.

of the parameter β on the decomposition and guidelines on choosing β for other FSI configurations, we refer the reader to Appendix D.

Fig. 10a and b show the computed spectral POD eigenvalues (normalized by the sum of eigenvalues) for both Re_τ at the first four peak frequencies in Fig. 3a. For $\beta = 0.01$, we observe that only the first eigenvalue is dominant, and it contributes to the entire double integral $\iint_{-\delta}^{+\delta} G(r,s,\beta/(1-\beta))/(1-\beta)\, \Gamma^a(r,s,\omega)\, \mathrm{d}r\, \mathrm{d}s$ (Eq. (29)).

Fig. 11a and b show the contribution of each spectral POD mode to the plate averaged displacement PSD (Eq. (30)) for the frequencies discussed in Table 6. The first spectral POD mode contributes nearly all the plate averaged displacement PSD at all frequencies for both Re_τ. Thus, the first spectral POD mode is the dominant decorrelated contributor to plate response at all the peak frequencies investigated. To investigate the structure of this dominant fluid source, we plot the envelope and phase of the first spectral POD mode in Fig. 13–14 for the frequencies plotted in Fig. 10. For all the Reynolds numbers and frequencies, the envelope is maximum in the buffer layer and the modes have a similar wall-normal width for both Re_τ. This again reaffirms the observation in the previous section that the contribution from the fluid sources peak in the buffer layer and its width extends up to the outer layer. The phase variation of these dominant modes is mostly in the range $-\pi/2$ to $\pi/2$. Thus, the contribution from different wall-parallel planes interfere constructively. This constructive interference is absent in the suboptimal spectral POD modes. Even though the second spectral POD mode

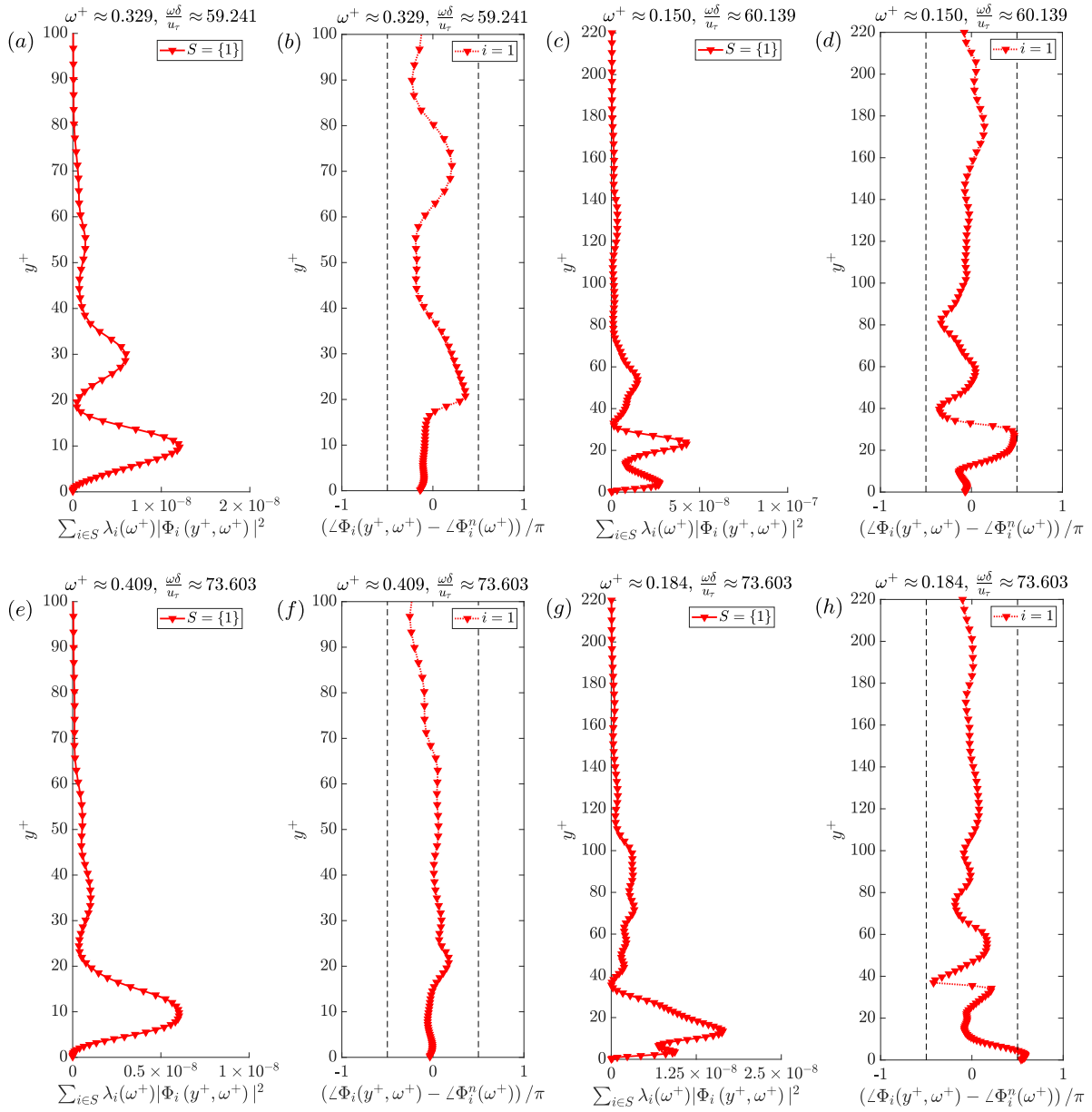

Fig. 14. Envelope ((a), (c), (e), (g)) and phase ((b), (d), (f), (h)) of the dominant spectral POD mode computed using the Poisson inner product ($\beta = 0.01$). Figures (a), (b), (c), and (d) are for the peak frequency $\omega\delta/u_\tau \approx 60$, and figures (e), (f), (g), and (h) are for the peak frequency $\omega\delta/u_\tau \approx 73$. Figures (a), (b), (e), and (f) are for $Re_\tau = 180$, and figures (c), (d), (g), and (h) are for $Re_\tau = 400$.

contains more energy than the first mode (Fig. 12), the contributions interfere destructively resulting in very small net contribution. Therefore, the interference of the contributions from different wall-parallel planes plays a major role in determining the dominance of a spectral POD mode.

Fig. 12 shows that the dominant spectral POD mode is not the dominant contributor to the integrated net displacement source PSD ($\int_{-\delta}^{+\delta} \Gamma^a(y, y, \omega)\,\mathrm{dy}$), i.e., they are not energetically dominant. The first two energetically dominant modes identified by the inner product with $\beta = 1$ (standard L^2 inner product) is shown in Fig. 15 for $\omega\delta/u_\tau \approx 50$. The shape of the modes resembles a stationary wavepacket enclosing a traveling wave (almost linear phase variation) for both Re_τ. However, these wavepackets do not contribute much to the response of the plate as the contribution from different wall-normal locations interfere destructively to produce no net contribution. This behavior of the energetically dominant mode is also true at higher frequencies (not shown). Further, the spectral POD modes identified by the inner-products with $\beta = 1$ (standard L^2 inner-product) and $\beta = 0.01$ are inherently different because they optimize the modes based on their

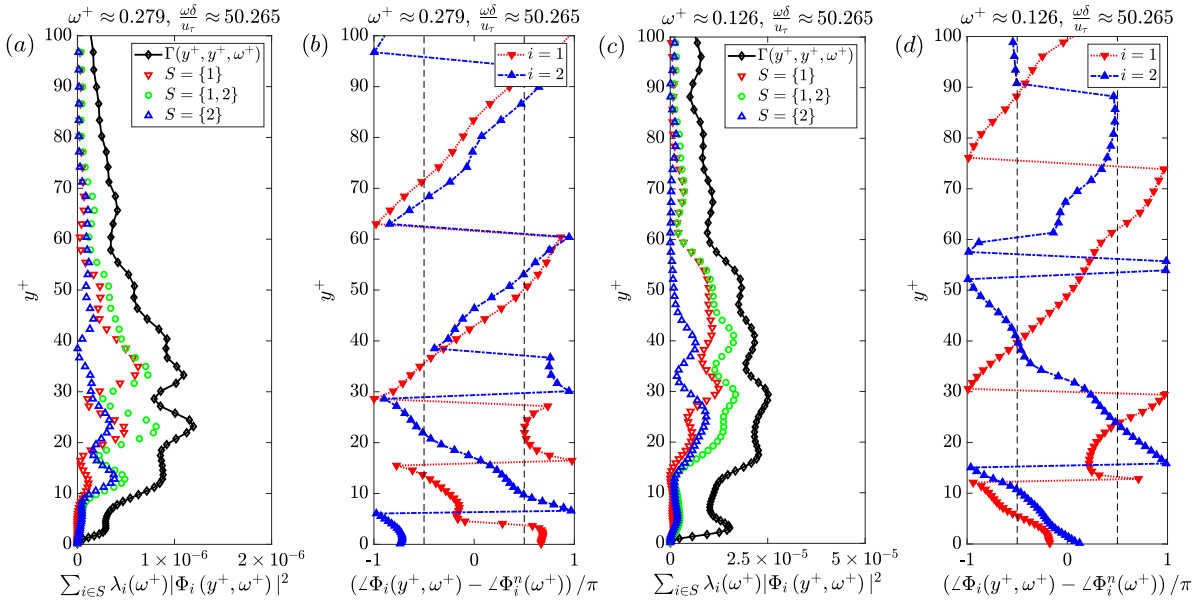

Fig. 15. Envelope and phase of the dominant spectral POD modes computed using the L^2 inner product for $Re_\tau = 180$ ((a)-envelope, (b)-phase) and $Re_\tau = 400$ ((c)-envelope, (d)-phase) at peak frequency $\omega\delta/u_\tau \approx 50.2$.

contribution to $\int_{-\delta}^{+\delta} \Gamma^a(y, y, \omega)\,\mathrm{d}y$ (Eq. (34)) and $\iint_{-\delta}^{+\delta} 1/(1-\beta)G(y, r, \beta/(1-\beta))\Gamma^a(r, y, \omega)\,\mathrm{d}r\,\mathrm{d}y$ (Eq. (29)), respectively. The former picks the energetically dominant mode whereas the latter identifies the mode that contributes the most to the double integral (which is a proxy for $\phi_{dd}^a(\omega)$).

Overall, spectral POD identifies a single dominant contributor to the plate excitation at each of the dominant resonant frequencies in Table 6. All the identified dominant plate excitation modes have an envelope that peaks in the buffer layer and has a width that extends up to the outer region of the channel for both Reynolds numbers. Further, the dominant plate excitation mode is not energetically dominant, i.e., it does not contribute much to the PSD $\Gamma^a(y, y, \omega)$. It is the constructive interference between the contributions from different wall-normal regions that leads to maximum contribution to the plate excitation.

5. Summary

In summary, we present a novel framework to investigate the fluid–solid coupling in a canonical setting — linear one-way coupled excitation of an elastic plate in turbulent channel flow. We apply the framework to explain the response of a clamped plate obtained using the in-house FSI solver — MPCUGLES-SOLID at $Re_\tau = 180$ and 400.

The obtained plate response at $Re_\tau = 180$ and 400 with fixed non-dimensional Young's modulus $E/(\rho_f u_\tau^2)$ have overlapping plate averaged low frequency spectrum in outer units. But, the high frequency component of the spectrum does not show overlap in inner units. Fixing $E\delta^2/(\rho_f \nu_f^2)$ instead of $E/(\rho_f u_\tau^2)$ for the two Re_τ yields a better collapse of the high-frequency region in inner units. We show that this high-frequency behavior is due to the modal wavenumber scaling better in inner units.

The resonant vibration at the first natural frequency is smaller than at the second natural frequency. The global maximum seems to occur at the third natural frequency. We understand this by comparing the streamwise fluid and solid length scales. For the solid length scale, we use the mode shape of the plate. For the fluid length scale, we use the CSD of the wall-pressure fluctuations. The differing values of the two length scales at the first natural frequency leads to smaller resonant vibration. At the second and third natural frequencies, the two length scales become comparable, leading to larger resonant vibration.

In the proposed fluid–solid coupling framework, we express the displacement at a point on the surface of the plate $d(x, -\delta, z, t)$ as a wall-normal integral of the net displacement source $f_d(x, y, z, t)$, i.e., $d(x, -\delta, z, t) = \int_{-\delta}^{+\delta} f_d(x, y, z, t)\,\mathrm{d}y$. To quantify the statistical features of fluid sources of plate excitation, we compute the plate averaged CSD of the net displacement source using the DNS database and modal superposition. We use the first 50 mode shapes of the plate to investigate the fluid sources.

The computed plate averaged wall displacement–net displacement source CSD $\Psi^a(y, \omega)$ is maximum in the buffer layer, indicating peak correlation with the plate response. The CSD extends well into the outer region of the channel. If we consider the integrated contribution from different regions of the channel to the plate response, the overlap and outer

regions also contribute significantly (50% for $Re_\tau = 180$ and 65% for $Re_\tau = 400$). Further, this overlap and outer region contribution appears to increase with Reynolds number.

We show that the Mellen form of the wavenumber frequency spectrum implies identical coupling of the plate averaged displacement PSD and the wall-pressure PSD with the fluid sources in the channel up to a multiplicative constant.

We perform spectral POD of the net displacement source CSD to identify the decorrelated dominant fluid sources responsible for the plate excitation. To accomplish this, we require the modes to be orthogonal in a Poisson inner product instead of the commonly used L^2 inner product. The envelope of the dominant spectral POD mode peaks in the buffer region for both Re_τ and its width extends into the outer region, reaffirming the previous observations from the wall displacement–net displacement source CSD $\Psi^a(r,\omega)$. From the phase of the mode, we observe that the dominance of such a fluid source is mainly due to the constructive interference of the contributions from different wall-parallel planes. However, this contribution is dominant only in terms of plate excitation, not energy. The energetically dominant fluid sources obtained from spectral POD with the L^2 inner product resemble stationary wall-normal wave packets. But these wavepackets do not contribute much to the plate excitation. This is because the contributions from different wall-normal locations to the plate response undergo destructive interference.

Overall, the framework presented here enables quantitative analysis of how different wall-normal regions contribute to plate response. The exact values of the contributions presented here are specific to the chosen plate dimensions, material properties and Reynolds number. In FSI simulations that use wall-modeled Large Eddy Simulation in the fluid domain, the first point in the fluid domain will be in the logarithmic layer. The proposed framework can be used to assess the significance of this missing buffer region contribution to the structural excitation. At very high Reynolds numbers, the contribution of the outer layer structures to the wall-pressure fluctuation increases (Panton et al., 2017). The framework proposed here can be used to quantitatively investigate this outer layer contribution to the plate excitation.

CRediT authorship contribution statement

Sreevatsa Anantharamu: Formal analysis, Writing - original draft. **Krishnan Mahesh:** Writing -review & editing, Supervision.

Declaration of competing interest

The authors declare that they have no known competing financial interests or personal relationships that could have appeared to influence the work reported in this paper.

Acknowledgments

This work is supported by the United States Office of Naval Research (ONR) under grant N00014-17-1-2939 with Dr. Ki-Han Kim as the technical monitor. The computations were made possible through computing resources provided by the US Army Engineer Research and Development Center (ERDC) in Vicksburg, Mississippi on the Cray machines, Copper and Onyx of the High Performance Computing Modernization Program. We also thank for the computing resources provided by the US Air Force Research Laboratory DoD Supercomputing Resource Center (DSRC) on the SGI ICE machine, Thunder of the High Performance Computing Modernization Program.

Appendix A. On the choice of the non-dimensional structural parameters

To arrive at the non-dimensional structural parameters in Table 3, we first start by setting the friction Reynolds number (Re_τ) to be 180. Then, we choose the dimensional values for the channel height (δ), fluid density (ρ_f) and kinematic viscosity (ν_f) to be 2.5×10^{-2} m, 1.28 kg m^{-3}, and 1.48×10^{-5} m^2 s^{-1}, respectively. The resulting friction velocity u_τ is 0.106 m s^{-1}. Finally, we choose the solid Young's modulus, density and Poisson's ratio to be 100 MPa, and 1500 kg m^{-3} and 0.4, respectively, and we arrive at the non-dimensional values in Table 3. For $Re_\tau = 400$, we use the same non-dimensional values to retain the same natural frequencies in outer units ($\omega\delta/u_\tau$).

Note that the fluid properties are that of air. The structural properties, except for the Poisson's ratio, are close to that of rubber, and the channel height is similar to the experiment of Zhang et al. (2017). We mainly choose a soft material with the above properties to have at least five natural frequencies in the low-frequency ($\omega^+ < 1$) range. In this way, we ensure the low-frequency structural response to be a combination of several mode shapes and not just the first mode. Stiffer materials like steel or aluminum would have led to the smallest natural frequency in the high-frequency range ($\omega^+ > 1$) for $Re_\tau = 180$ and 400. The resulting low-frequency structural response that would make up most of the root-mean-square would only depend on the first mode shape and not a combination of different modes. Multi-modal contribution to the low frequency excitation for stiff materials requires higher Reynolds number.

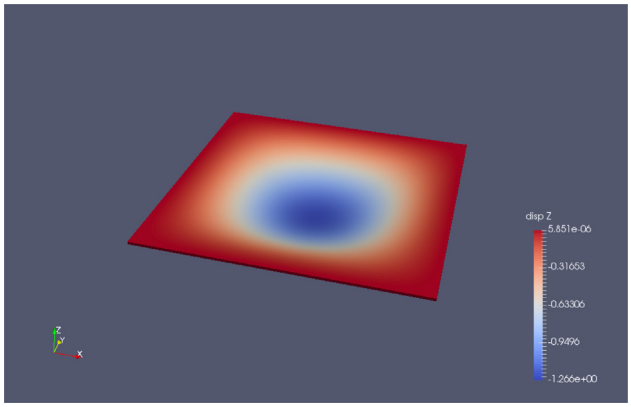

Fig. 16. Static deformation of a clamped plate.

Table 8
Comparison of the non-dimensional numerical plate center displacement $\frac{w_c}{qL^4/D}10^3$ to Taylor and Govindjee (2004).

Number of dofs	Reference	Numerical
729	1.27	0.9
2601	1.27	1.18
9801	1.27	1.24
38 025	1.27	1.26
17.3×10^6	1.27	1.27

Table 9
Comparison of the non-dimensional natural frequencies $\omega_n\sqrt{\frac{\rho_S h}{D}}L^2$ to Leissa (1969).

Mode	Reference	Numerical
1	36	36.08
2	73.41	73.58
3	73.41	73.58
4	108.3	108.4
5	131.6	131.92

Appendix B. Structural solver validation

We validate the structural solver for static, eigenvalue, and dynamic problems for an elastic square plate clamped on all the four sides. For all the validation cases, we discretize the solid geometry with uniform 27-node hexahedral elements. We choose the length and width of the plate (a) to be 10 and thickness (h) to be 0.1. We set the Young's modulus (E) and the Poisson's ratio (ν) to be 10.92×10^5 and 0.3, respectively and obtain a bending stiffness ($D=Eh^3/(12(1-\nu^2))$) of 100.

Fig. 16 shows the static deformation of the plate with a uniform pressure loading of $q=-10$. We compare the obtained non-dimensional plate center displacement $\frac{w_c}{D/(qa^4)}10^3$ to the reference result of Taylor and Govindjee (2004), where w_c is the plate center displacement. Table 8 shows good agreement and convergence with increase in number of degrees of freedom. Note that the reference results of Taylor and Govindjee (2004) solve the Poisson–Kirchhoff plate theory equations using spectral method where as we solve the 3D elasticity equations without thin plate theory assumptions.

Table 9 compares the computed eigenvalues of the first five modes of the clamped square plate to the reference results compiled by Leissa (1969). We use 32 elements in each direction parallel to the plane of the plate and 1 element along the plate thickness. We observe good agreement between the solver and the reference results. Fig. 17 shows the computed mode shapes of the clamped plate.

To build confidence on the amplitude of the vibrations obtained from the solver, we validate the solver for a forced vibration problem. The plate dimension and mesh are the same as that used in the eigenvalue validation. To restrict the excitation only to the first mode of vibration, we define the spatial form of the force vector to be $M\{\varphi_1\}sin(\omega t)$, where M is the mass matrix, $\{\varphi_1\}$ is the degree of freedom vector of the first mode of vibration, and ω is the excitation frequency. We choose the nondimensional excitation frequency $\omega\sqrt{\frac{\rho h}{D}}L^2$ to be 10. The response of such a forcing will only have a component ($d_1(t)$) along the first mode of vibration, i.e., the resulting displacement degree of freedom vector will be $d_1(t)\{\varphi_1\}$. Note that $d_1(t)$ is a scalar function of time which we can compute analytically using the Duhamel integral

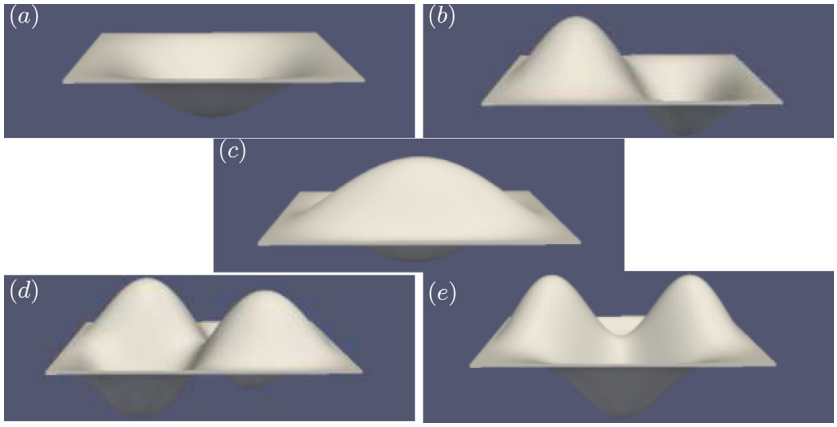

Fig. 17. (a) First, (b) second, (c) third, (d) fourth, and (e) fifth mode shape of the clamped plate.

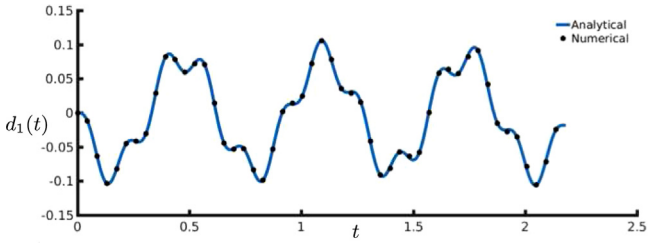

Fig. 18. Comparison of numerically obtained component of the response along the first mode of vibration to the analytical result.

(Bathe, 2006). We compare the analytical result to the obtained simulation results in Fig. 18. We observe good agreement between the two. This validates the accuracy of the amplitude of the vibrations obtained from the solver.

Appendix C. On the choice of the number of modes to compute the net displacement source CSD

We verify below that 50 modes of the plate are sufficient to analyze the plate excitation sources for frequencies smaller than $\omega\delta/u_\tau = 500$. We do so by comparing the plate averaged displacement spectrum computed directly from the one-way coupled DNS to that obtained from the net displacement source CSD using Eq. (4). Fig. 19a and b show this comparison for $Re_\tau = 180$ and 400, respectively. Red symbols denote the spectrum computed from the one-way coupled DNS and solid black lines denote the net displacement source CSD Γ^a. The two spectra agree for $\omega\delta/u_\tau < 500$. Therefore, 50 modes are sufficient. For higher frequencies, the spectrum computed using the net displacement source CSD decays much rapidly. This rapid decay is because of the absence of modes with indices higher than 50. These higher mode shapes need to be accounted to investigate even higher frequencies.

For the current example, this reasoning and the choice of the number of modes are valid for both Reynolds numbers. This is because the material parameters are the same in outer units for both Re_τ. This similarity leads to identical natural frequencies and mode shapes. Hence, the same number of modes are required to account for the contribution from frequencies smaller than $\omega\delta/u_\tau = 500$ for both Re_τ.

If the material parameters remain fixed in outer units, then for increasing Reynolds numbers, 50 modes would still be sufficient to analyze the sources in the same frequency range. However, suppose one chooses a different set of material parameters or a different upper bound on the frequency range in outer units. Then, the number of modes required to compute the CSD is no longer equal to 50.

We present below the guidelines to choose the number of modes to compute the net displacement source CSD for the general case (any Reynolds number and material parameters). First, choose an upper bound ω_{ub}/ω_{ref} for the frequencies of interest. Here, ω_{ref} is the chosen frequency scale. Then, perform eigenanalysis of the plate to identify the smallest mode-index j_{min} whose non-dimensional natural frequency $\omega_{j_{min}}/\omega_{ref}$ is larger than the chosen upper bound ω_{ub}/ω_{ref}. j_{min} would then be the minimum number of modes required to compute the net displacement source CSD. Finally, verify this number by comparing the spectrum computed using Γ^a to that obtained using the one-way coupled DNS and add more modes, if required. For the current example, $\omega_{ref} = u_\tau/\delta$, $\omega_c = 500$ and $\omega_{50}\delta/u_\tau = 552$.

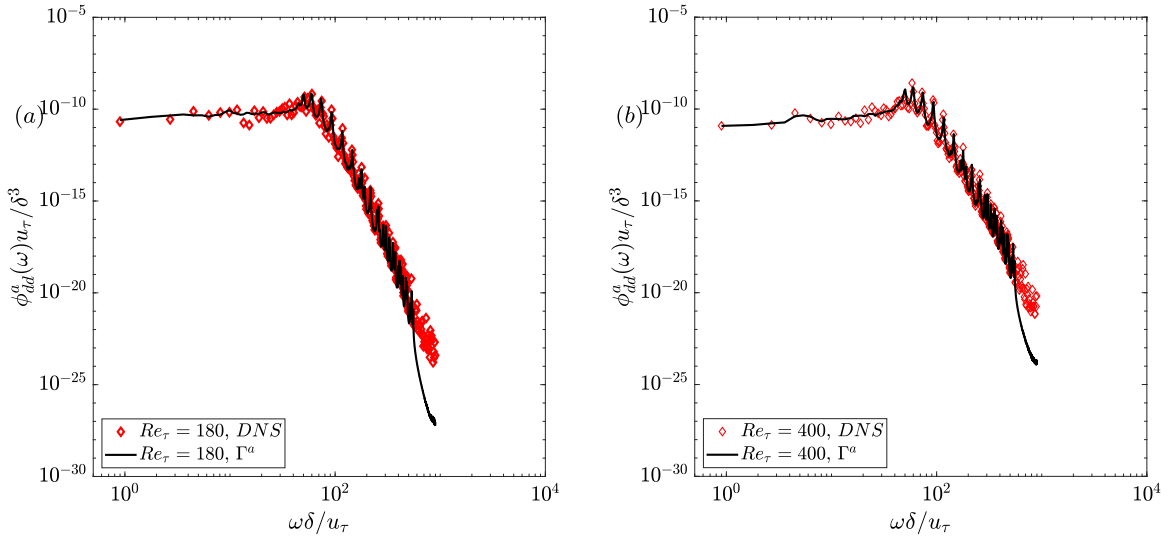

Fig. 19. Comparison of the plate averaged displacement spectrum computed from the CSD Γ^a using Eq. (4) to that obtained from DNS for (a) $Re_\tau = 180$ and (b) $Re_\tau = 400$. (For interpretation of the references to color in this figure legend, the reader is referred to the web version of this article.)

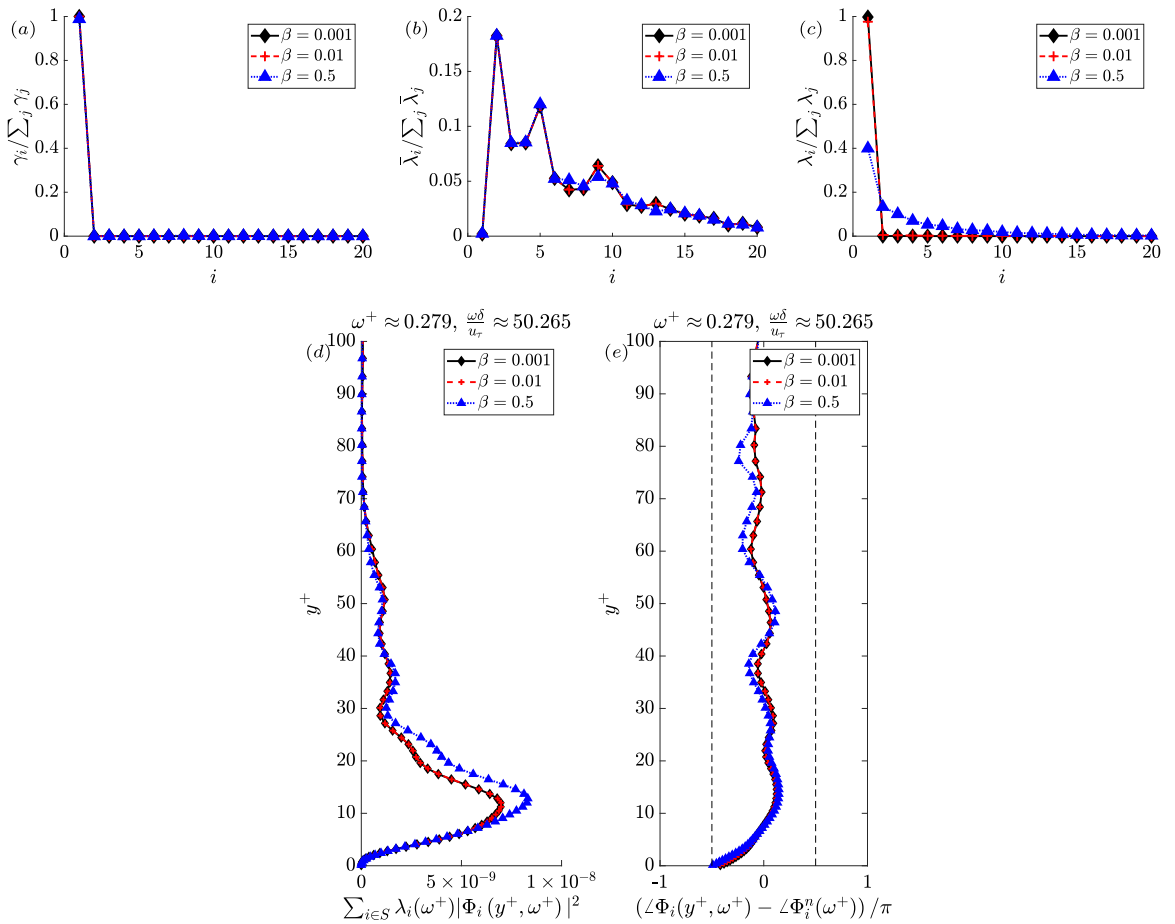

Fig. 20. Figure (a) compares the fractional contribution of each spectral POD mode to the plate averaged displacement spectrum for different values of β. Figure (b) compares the fractional contribution of each spectral POD mode to the integrated net displacement source PSD. Figure (c) compares the spectral POD eigenvalues for different values of β. Figures (d) and (e) show the envelope and phase of the dominant spectral POD mode for different values of β. All the plots are for $Re_\tau = 180$ at $\omega\delta/u_\tau = 50.2$.

Appendix D. On the choice of the parameter β in spectral POD

The influence of the value β on the reported spectral POD results is shown in Fig. 20 for $Re_\tau = 180$ at $\omega\delta/u_\tau = 50.2$. The curves for $\beta = 0.01$ and 0.001 overlap in each figure. This shows that $\beta = 0.01$ is sufficiently small to extract the same dominant plate excitation mode as $\beta = 0.001$. For $\beta = 0.5$, we observe some differences in the eigenvalues (Fig. 20c) and the mode shapes (Fig. 20d, e). However, the dominant mode still accounts for the entire plate excitation and has very similar shape to the other values of β.

Overall, we observe that the spectral POD modes appear to converge as we decrease β. We chose $\beta = 0.01$ because the results did not noticeably change by decreasing β to 0.001. We observed this behavior at other frequencies and Reynolds number.

To understand this dependence of the results on β, recall Eq. (29),

$$\int\int_{-\delta}^{+\delta} \frac{G\left(r, s, \frac{\beta}{1-\beta}\right)}{1-\beta} \Gamma^a(r, s, \omega)\, \mathrm{d}r\, \mathrm{d}s = \sum_{j=1}^{\infty} \lambda_j(\omega). \tag{55}$$

As we decrease the value of β, $\beta/(1-\beta)$ becomes smaller and the Green's function $G(r, s, \beta/(1-\beta))$ becomes flatter in r and s. In other words, the Green's function becomes nearly constant. Hence, for very small values of β, the left hand side of Eq. (29) converges to $\int\int_{-\delta}^{+\delta} \Gamma^a(r, s, \omega)\, \mathrm{d}r\, \mathrm{d}s$ (up to a multiplicative constant). Therefore, the resulting modes and eigenvalues also converge.

In general, for other FSI configurations, one should choose a small value of β to isolate sources responsible for structural excitation. The value $\beta = 0.01$ is not universal. To arrive at a suitable value for β, one should first compare the results obtained with several small values of β. Then, choose β to be the value for which the modes seem converged. Also, note that β cannot be zero because then, the kernel of the Poisson inner product would not be symmetric and positive definite.

References

Anantharamu, S., Mahesh, K., 2020. Analysis of wall-pressure fluctuation sources from direct numerical simulation of turbulent channel flow. J. Fluid Mech. 898.

Bathe, K.J., 2006. Finite Element Procedures. Klaus-Jurgen Bathe.

Bendat, J.S., Piersol, A.G., 2011. Random Data: Analysis and Measurement Procedures, Vol. 729. John Wiley & Sons.

Bernardini, M., Pirozzoli, S., Quadrio, M., Orlandi, P., 2013. Turbulent channel flow simulations in convecting reference frames. J. Comput. Phys. 232 (1), 1–6.

Blake, W.K., 2017. Mechanics of Flow-Induced Sound and Vibration, Volume 1 and 2. Academic Press.

Bull, M.K., 1967. Wall-pressure fluctuations associated with subsonic turbulent boundary layer flow. J. Fluid Mech. 28 (4), 719–754.

Chang III, P.A., Piomelli, U., Blake, W.K., 1999. Relationship between wall pressure and velocity-field sources. Phys. Fluids 11 (11), 3434–3448.

Chase, D.M., 1980. Modeling the wavevector-frequency spectrum of turbulent boundary layer wall pressure. J. Sound Vib. 70 (1), 29–67.

Corcos, G.M., 1964. The structure of the turbulent pressure field in boundary-layer flows. J. Fluid Mech. 18 (3), 353–378.

Farabee, T.M., Casarella, M.J., 1991. Spectral features of wall pressure fluctuations beneath turbulent boundary layers. Phys. Fluids A 3 (10), 2410–2420.

Ghaemi, S., Scarano, F., 2013. Turbulent structure of high-amplitude pressure peaks within the turbulent boundary layer. J. Fluid Mech. 735, 381–426.

Goody, M., 2004. Empirical spectral model of surface pressure fluctuations. AIAA J. 42 (9), 1788–1794.

Hambric, S.A., Hwang, Y.F., Bonness, W.K., 2004. Vibrations of plates with clamped and free edges excited by low-speed turbulent boundary layer flow. J. Fluids Struct. 19 (1), 93–110.

Hoyas, S., Jiménez, J., 2006. Scaling of the velocity fluctuations in turbulent channels up to $Re_\tau = 2003$. Phys. Fluids 18 (1), 011702.

Hu, Z., Morfey, C.L., Sandham, N.D., 2006. Wall pressure and shear stress spectra from direct simulations of channel flow. AIAA J. 44 (7), 1541–1549.

Hwang, Y.F., 1998. A discrete model of turbulence loading function for computation of flow-induced vibration and noise. In: Proceedings of the ASME International Mechanical Engineering Congress and Exposition, Anaheim, CA.

Hwang, Y.F., Maidanik, G., 1990. A wavenumber analysis of the coupling of a structural mode and flow turbulence. J. Sound Vib. 142 (1), 135–152.

Klöppel, T., Gee, M.W., Wall, W.A., 2011. A scaled thickness conditioning for solid-and solid-shell discretizations of thin-walled structures. Comput. Methods Appl. Mech. Engrg. 200 (9–12), 1301–1310.

Leissa, A.W., 1969. Vibration of Plates. Technical Report, Ohio State University, Columbus, Ohio.

Li, X.S., Demmel, J.W., 2003. Superlu_dist: A scalable distributed-memory sparse direct solver for unsymmetric linear systems. ACM Trans. Math. Softw. (TOMS) 29 (2), 110–140.

Mahesh, K., Constantinescu, G., Moin, P., 2004. A numerical method for large-eddy simulation in complex geometries. J. Comput. Phys. 197 (1), 215–240.

Panton, R.L., Lee, M., Moser, R.D., 2017. Correlation of pressure fluctuations in turbulent wall layers. Phys. Rev. Fluids 2 (9), 094604.

Pope, S.B., 2001. Turbulent Flows. Cambridge University Press.

Rosti, M.E., Brandt, L., 2017. Numerical simulation of turbulent channel flow over a viscous hyper-elastic wall. J. Fluid Mech. 830, 708–735.

Smol'Iakov, A.V., Tkachenko, V.M., 1991. Models of a field of pseudoacoustic turbulent wall pressures and experimental data. Akust. Zh. 37, 1199–1207.

Taylor, R.L., Govindjee, S., 2004. Solution of clamped rectangular plate problems. Int. J. Numer. Methods Biomed. Eng. 20 (10), 757–765.

Zhang, C., Wang, J., Blake, W., Katz, J., 2017. Deformation of a compliant wall in a turbulent channel flow. J. Fluid Mech. 823, 345–390.